Aalborg University

# Modelling and Implementation of Active Thermal Control Methods for Power Electronics Systems for Motor Drive Applications

AALBORG UNIVERSITET

Department of Energy Technology

PED4-1047

Master Student: Ionuț Vernica

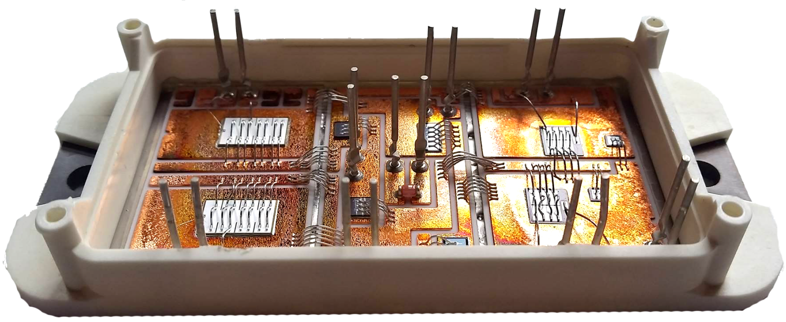

June 2016

**Title:** Modelling and Implementation of Active Thermal Control Methods for Power Electronics Systems for Motor Drive Applications
**Semester:** $10^{th}$
**Semester theme:** Master Thesis
**Project period:** 01.02.16 to 01.06.16
**ECTS:** 30
**Supervisor:** Ke Ma and Frede Blaabjerg
**Project group:** PED4 - 1047


Ionuț Vernica


Pages, total: 49
Appendix: -
Copies: 4


**SYNOPSIS:**

The main objective of this thesis consists of modelling and implementing active thermal control methods, in order to reduce the large thermal cycling which occurs in the power devices of a motor drive application. The motor drive system together with the thermal loading of the power devices have been modelled, and the dynamic behavior of the system has been analyzed. Three active control methods have been proposed and their impact during the deceleration period of the motor has been investigated. A mission profile emulation algorithm has been developed for a three level NPC H-bridge. Finally, the simulation results have been validated by means of experimental work.

# Contents


**Contents** **i**

**List of Figures** **iii**

**1 Introduction** **1**
- 1.1 Background Information . . . . . . . 1
- 1.2 Problem Formulation . . . . . . . 2
- 1.3 Project Objectives . . . . . . . 4
- 1.4 Project Limitations . . . . . . . 5

**2 Modelling of Thermal Cycling** **6**
- 2.1 Permanent Magnet Synchronous Machine . . . . . . . 7
  - 2.1.1 Field Oriented Control . . . . . . . 9
  - 2.1.2 PI Controller Design . . . . . . . 10
- 2.2 Voltage Source Inverter . . . . . . . 16
  - 2.2.1 Discontinuous Pulse Width Modulation . . . . . . . 17
- 2.3 Power Loss Model . . . . . . . 19
  - 2.3.1 Conduction Losses . . . . . . . 20
  - 2.3.2 Switching Losses . . . . . . . 21
  - 2.3.3 Temperature Dependency . . . . . . . 22
- 2.4 Thermal Model . . . . . . . 23
- 2.5 Simulation Results . . . . . . . 25

**3 Active Thermal Control for Improved Lifetime of Power Devices** **29**
- 3.1 Switching Frequency Adjustment . . . . . . . 30
- 3.2 Reactive Current Injection . . . . . . . 31
- 3.3 Deceleration Slope Adjustment . . . . . . . 32

**4 Experimental Validation** **35**
- 4.1 Laboratory Setup . . . . . . . 35
- 4.2 Mission Profile Emulation . . . . . . . 38
  - 4.2.1 Motor Drive Mission Profile . . . . . . . 38
  - 4.2.2 Orthogonal Signal Generator . . . . . . . 39
  - 4.2.3 Current Controller . . . . . . . 40
- 4.3 Simulation and Experimental Results . . . . . . . 42

**5 Conclusions** **48**
- 5.1 Future work . . . . . . . 48

**Bibliography** **50**

# List of Figures


1.1 System circuit diagram . . . 1
1.2 PV component failure rates . . . 2
1.3 WTS component failure rates . . . 2
1.4 Individual component failure rates . . . 3
1.5 Stress on electronic equipment . . . 3
1.6 Bond wire lift-off . . . 3
1.7 Chip solder crack . . . 3
1.8 Effect of current on thermal cycling . . . 4
1.9 Effect of frequency on thermal cycling . . . 4

2.1 Overview of the system model . . . 6
2.2 Cross section view . . . 7
2.3 Equivalent electrical circuit . . . 7
2.4 d-axis equivalent circuit . . . 8
2.5 q-axis equivalent circuit . . . 8
2.6 Field oriented control block diagram . . . 9
2.7 $i_q$ current control loop . . . 11
2.8 $i_q$ Current loop with unity feedback . . . 11
2.9 Bode diagram - $i_q$ control loop . . . 12
2.10 Step response - $i_q$ control loop . . . 12
2.11 Speed control loop . . . 13
2.12 Speed loop with unity gain feedback . . . 14
2.13 Bode diagram - $\omega_e$ control loop . . . 15
2.14 Step response - $\omega_e$ control loop . . . 15
2.15 Bode diagram - $\omega_e$ control loop . . . 15
2.16 Step response - $\omega_e$ control loop . . . 15
2.17 PI regulator with anti-windup . . . 16
2.18 Three phase VSI . . . 16
2.19 DPWM1 technique . . . 18
2.20 Zero sequence signal . . . 18
2.21 Control voltage . . . 18
2.22 Diode switching characteristic . . . 19
2.23 IGBT switching characteristic . . . 19
2.24 Diode forward voltage curve . . . 20
2.25 MOSFET drain-source voltage curve . . . 20
2.26 MOSFET switching energy at $25^oC$ . . . 21
2.27 MOSFET switching energy at $125^oC$ . . . 21
2.28 Diode reverse recovery curve . . . 22
2.29 MOSFET On/Off switching energy . . . 22
2.30 Power loss model diagram . . . 23
2.31 Foster RC thermal network . . . 24
2.32 Diode thermal impedance . . . 24

2.33 MOSFET thermal impedance . . . . . 24
2.34 Thermal model diagram . . . . . 25
2.35 Speed mission profile . . . . . 25
2.36 Torque mission profile . . . . . 25
2.37 Rotor speed & torque of the PMSM . . . . . 26
2.38 $i_q$ & $i_d$ Currents . . . . . 26
2.39 Phase voltages . . . . . 26
2.40 Phase currents . . . . . 26
2.41 Conduction and switching losses . . . . . 27
2.42 Total losses in power device . . . . . 27
2.43 Junction temperature of the power device . . . . . 28

3.1 Look-up table based active thermal control . . . . . 30
3.2 Power device losses . . . . . 31
3.3 Power device junction temperature . . . . . 31
3.4 $i_d$ and $i_q$ currents . . . . . 32
3.5 Phase currents . . . . . 32
3.6 Total power losses of the device . . . . . 32
3.7 Power device junction temperature . . . . . 32
3.8 Speed & Torque response of the motor . . . . . 33
3.9 Phase currents . . . . . 33
3.10 Total power losses of the device . . . . . 33
3.11 Power device junction temperature . . . . . 33

4.1 Experimental setup . . . . . 35
4.2 Experimental setup block diagram . . . . . 35
4.3 H-bridge NPC inverter . . . . . 36
4.4 Circuit diagram of H-bridge NPC . . . . . 36
4.5 Protection board . . . . . 37
4.6 NPC interface board . . . . . 37
4.7 IGBT open module . . . . . 37
4.8 IGBT open module bridge . . . . . 37
4.9 dSpace - Simulink model . . . . . 38
4.10 Mission Profile Emulation block diagram . . . . . 39
4.11 Transport Delay . . . . . 40
4.12 Second Order Generalized Integrator . . . . . 40
4.13 Variable transport delay . . . . . 40
4.14 SOGI . . . . . 40
4.15 Current control loop . . . . . 41
4.16 Current Control - Bode Diagram . . . . . 41
4.17 Current Control - Step Response . . . . . 41
4.18 Test leg PWM . . . . . 42
4.19 Inverter output voltage . . . . . 42
4.20 Normal operation - Mission profile . . . . . 42
4.21 Normal operation mission profile . . . . . 43
4.22 Deceleration Slope Adjustment - Mission profile . . . . . 44

4.23 Decreased deceleration slope mission profile . . . . . . . . . . . . . . . . . . . . . . 45
4.24 Reactive Current Injection - Mission profile . . . . . . . . . . . . . . . . . . . . . . 45
4.25 Reactive current injection mission profile . . . . . . . . . . . . . . . . . . . . . . . 46
4.26 Reactive Current Injection - Mission profile . . . . . . . . . . . . . . . . . . . . . . 47
4.27 Zoomed View - Constant speed . . . . . . . . . . . . . . . . . . . . . . . . . . . . 47

5.1 IGBT open module . . . . . . . . . . . . . . . . . . . . . . . . . . . . . . . . . . 49

# Chapter 1

# Introduction

*Within the introduction chapter of this thesis, some background information will first be presented, followed by a detailed description of the problem which this project aims to solve. Afterwards, the project objectives are formulated and the chapter ends with the presentation of the thesis limitations and assumptions.*

## 1.1 Background Information

Nowadays, electrical machines are being widely used in a large variety of applications, from home appliances to renewable energy sources. Due to their high efficiency and relatively simple structure and control, three phase electric machines are commonly employed in the industry, in applications such as pump drives, fans or ventilation systems. Induction Machines (IM) represent the vast majority of three phase AC machines used worldwide, but in recent years, the use of Permanent Magnet Synchronous Machines (PMSM) has significantly increased, because of their high power density, in comparison with asynchronous machines [1].

In variable frequency drives, the PMSM will be fed by a power converter, which can assure the control of the machine over the full speed range by adjusting the magnitude and frequency of the modulated sinusoidal waveform. Additionally, if the application requires the machine to operate as a generator at certain times, thus injecting power into the grid, a back-to-back converter topology is used. This topology can usually be seen in wind power generating systems, but it is also commonly associated with high performance motor drives, in which regenerative braking is needed.

In this thesis, a PMSM driven by a back-to-back Voltage Source Converter (VSC) will represent the study case. The circuit diagram of the system is shown in Figure 1.1.

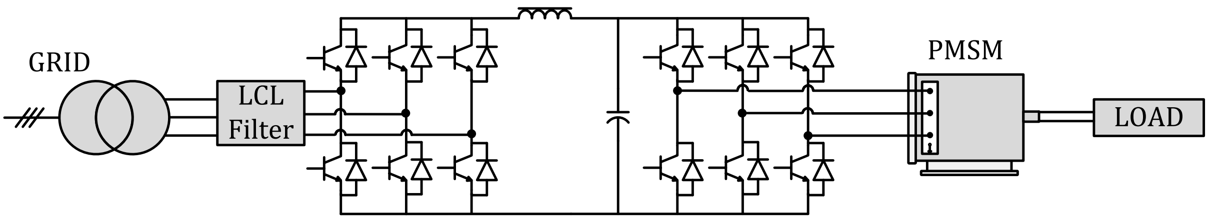


FIGURE 1.1: System circuit diagram

It is clear that during the *Motor Mode* operation of the machine, the grid side converter will act like a rectifier, converting the AC grid voltage to a constant DC voltage, while the machine side converter will supply a sinusoidal voltage to the terminals of the PMSM, according to the speed and torque requirements. On the other hand, when the machine operates in *Generator Mode*, the power will flow from the PMSM towards the grid, thus the machine side converter will behave as a rectifier, while the grid side converter will be used in order to inject a constant amplitude and frequency voltage into the grid.

Therefore, the essential role that the power converter has within the motor drive system can be highlighted, and it can be concluded that the overall efficiency and cost of the system are dependent on the reliability of the power converter.

## 1.2 Problem Formulation

In recent years, numerous studies have been carried out in order to analyze the reliability of power converters. In [2], the failure information and statistics of a Photovoltaic (PV) plant, operating in the field within a 5 year time margin, has been studied, and it has been concluded that the inverter represents one of the main critical components of the system. As it can be seen in Figure 1.2, the maintenance required by the inverter over the 5 year period, represents approximately 37% of the total number of unexpected maintenance events. Furthermore, by taking into consideration the maintenance cost, the necessity of improving the reliability of the inverter becomes crucial, in order to minimize the down time and the overall maintenance cost of the PV plant.

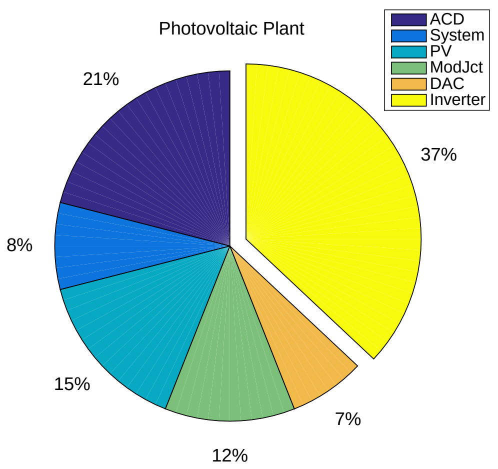


Figure 1.2: PV component failure rates

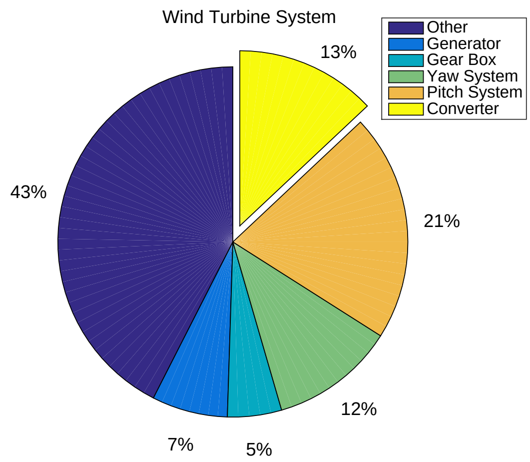


Figure 1.3: WTS component failure rates

A similar conclusion can be drawn by analyzing the failure rates which occur in Wind Turbine Systems (WTS). The study conducted in [3] has shown that 13% of the total failures are due to the power converter. The failure distribution rates in wind turbine systems can be seen in Figure 1.3.

In order to fully understand the main causes behind the high failure rates of power converters, an in-depth reliability survey has been carried out in [4]. The survey focused on the individual reliability of the electrical components of a general application power electronic converter. The results are shown in Figure 1.4 and it can be observed that the power semiconductor devices and the capacitors are the most fragile components of the power electronic system. Thus, by improving the lifetime of the power devices, the overall reliability of the power converter can be significantly increased.

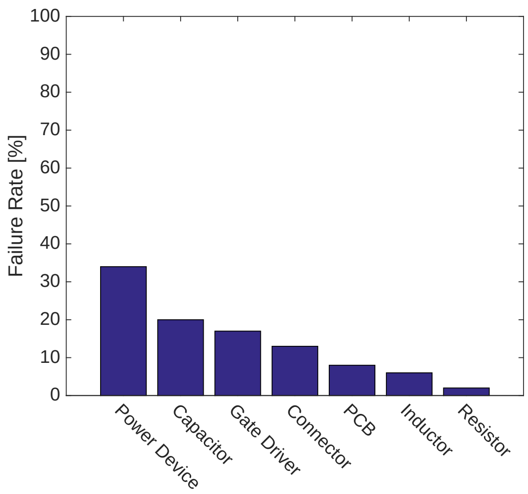


Figure 1.4: Individual component failure rates

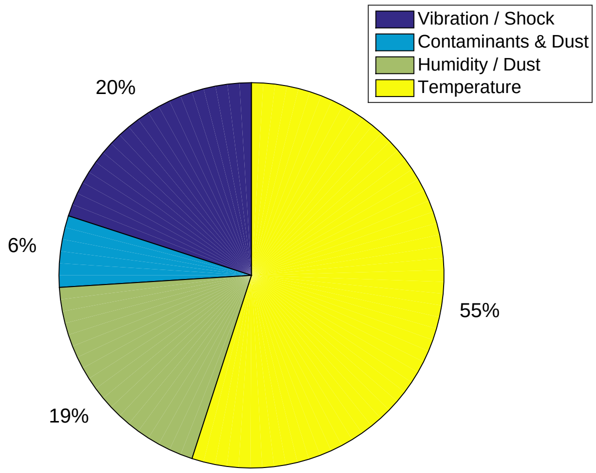


Figure 1.5: Stress on electronic equipment

The first step towards improving the reliability of the power devices is to correctly identify the failure mechanisms they are subject to and the root failure causes. According to [5], the predominant source of stress in electronic equipment is the steady state and cyclical temperature, which accounts for approximately 55% of the total stress, as shown in Figure 1.5.

Since the failure mechanisms may vary from one component to another due to their different structures, only a short overview of the most frequent failure mechanisms which appear in Insulated Gate Bipolar Transistor (IGBT) modules will be given. IGBT modules are commonly employed in many practical applications due to their high robustness and they also represent the given power module choice for the system study case analyzed throughout this thesis.

As presented in [6]-[7], two of the most common failures in IGBT modules, bond wire fatigue and solder fatigue, are caused by the thermal cycling which occurs in the module due to the load variation of the power converter or environmental temperature changes. Under adverse thermal stress, the Coefficient of Thermal Mismatch (CTM) between the bond wires and chip will lead to bond wire lift-off, as shown in Figure 1.6. Similarly, the thermo-mechanical stress induced by the CTE and thermal cycling can cause the appearance of cracks in the solder between the chip and the Direct Copper Bonded (DCB) substrate, phenomenon which can be seen in Figure 1.7.

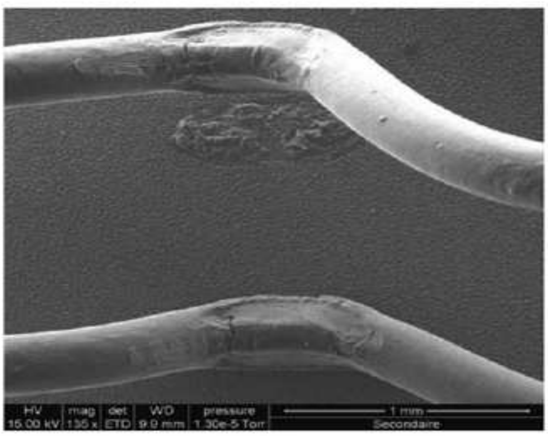

Figure 1.6: Bond wire lift-off [7]

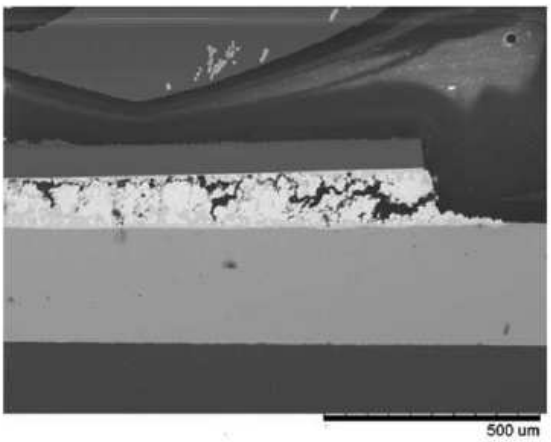


Figure 1.7: Chip solder crack [7]

The aforementioned failure mechanisms can also be frequently seen in the power electronic systems of motor drive applications. During the start-up and braking periods of the motor, the large amplitude of the current and the fact that the machine operates at low fundamental frequency can lead to high temperature swings in the power semiconductor devices [8]. The effect of the current amplitude and fundamental frequency on the thermal cycling of the power device is shown in Figure 1.8, respectively Figure 1.9. If not handled in a controlled manner, these large thermal cycles can result in a faster wear-out of the power devices, thus decreasing the reliability performance of the motor drive.

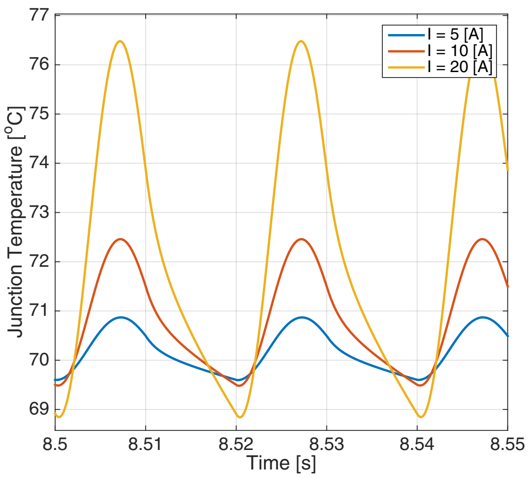


FIGURE 1.8: Effect of current on thermal cycling

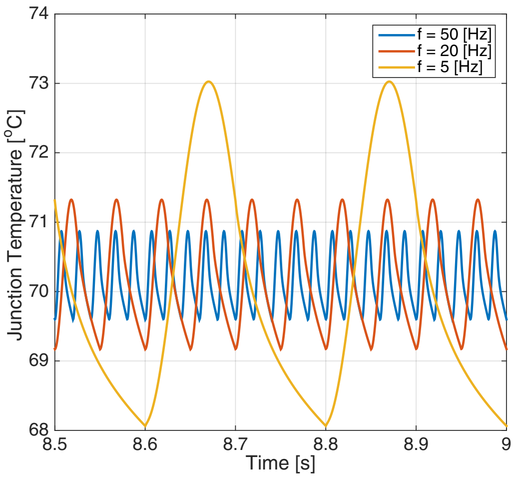


FIGURE 1.9: Effect of frequency on thermal cycling

## 1.3 Project Objectives

In the previous section, the adverse impact of the thermal cycling on the reliability of the power semiconductor devices has been highlighted. Therefore, in order to solve the prior mentioned problem and improve the lifetime of the power devices and the overall reliability performance of the system, the necessity of implementing an active thermal control method arises.

In this thesis, an active thermal control method based on adjusting the crucial parameters that influence the thermal behavior of the power devices is proposed. Hence the thesis objectives can be set as follows:

- *Model the electrical and thermal loading of the power devices based on certain motor drive mission profiles.*
- *Identify the main parameters that affect the thermal loading of the power devices.*
- *Develop and implement a mission profile emulation algorithm for the experimental setup.*
- *Model and implement various active thermal control methods.*
- *Analyze the effectiveness of the methods by means of power device lifetime estimation.*

## 1.4 Project Limitations

Due to time constrains, the following limitations need to be taken into consideration:

- The thermal loading of the grid side power devices will not be analyzed.
- The case and heat sink thermal behaviour of the power devices will not be modelled.
- Only the adverse thermal cycles which appear during the deceleration period of the motor will be analyzed.

Based on the above mentioned limitations, the following assumptions are made:

- The DC link voltage is constant and controllable.
- The case and heat sink temperatures are constant ($T_c = 65[^oC]$, $T_h = 52[^oC]$).

# Chapter 2

# Modelling of Thermal Cycling

*In this chapter a detailed description of the system models will be given. First, the three phase PMSM is introduced, together with the dq reference frame equations. Afterwards, the control strategy used in order to drive the motor will be presented, followed by the PI controller design procedure. Next, the mathematical model of the two level VSC is derived and the Discontinuous Pulse Width Modulation (DPWM) technique used to generate the gate drive signals will be shown. The equations which describe the power loss model will be emphasized. Finally, the thermal loading of the power devices will be modelled and the simulation results will be presented.*

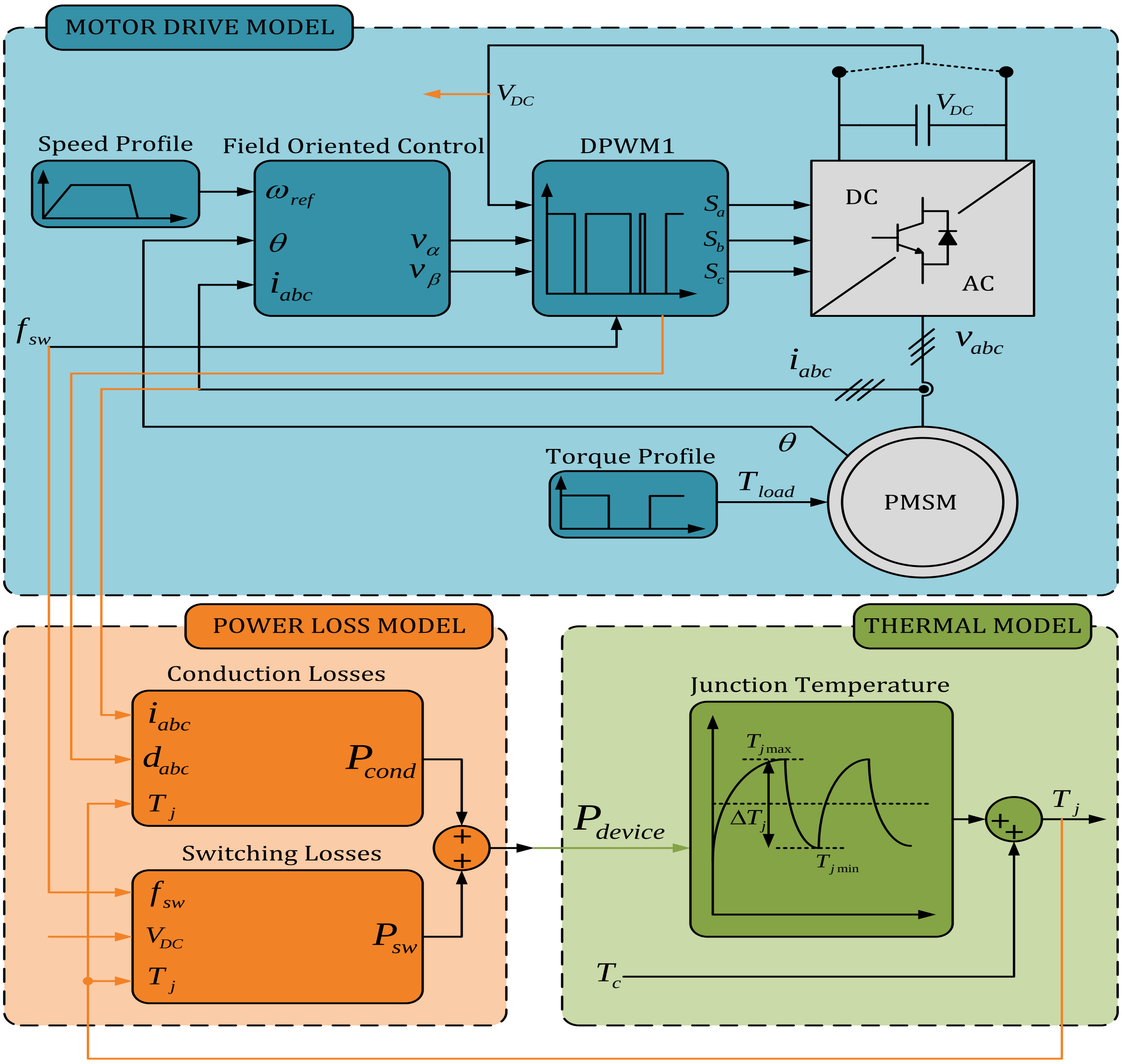


FIGURE 2.1: Overview of the system model

As illustrated in Figure 2.1, the system model is divided in three main sectors: motor drive model, power loss model and thermal model. The motor drive model analyses the dynamic behaviour of the PMSM under given speed and torque mission profiles. The outputs of the electrical circuit represent the inputs for the power loss calculation model, which will determine the conduction and switching losses of the power devices. Afterwards, the power losses which occur in in the power semiconductor devices can be translated to thermal stress by the thermal model. Each block from Figure 2.1 will be presented in detail.

## 2.1 Permanent Magnet Synchronous Machine

Due to their high efficiency, permanent magnet synchronous machines are attracting more and more attention and are being widely used in high performance applications. In comparison to the induction machine, where the rotor speed is always lower than the synchronous speed, the permanent magnets placed on the rotor will generate a constant magnetic field, thus forcing the motor to run at synchronous speed, independent of the load. The absence of slip rings and brushes give the PMSM a more simpler structure and will reduce the required maintenance time. The high efficiency of the PMSM is mainly due to the fact that there are no windings on the rotor, which will result in lower overall losses. The main drawbacks for this machine type are the high cost and the fact that the permanent magnets are subject to demagnetization when the machine operates in high temperature conditions [9].

During this project a 9.2 [kW] three phase PMSM is being used. This particular motor is designed to be used mainly in pump drive applications. The machine parameters can be seen Table 2.1 and the cross section of a single pole PMSM is shown in Figure 2.2:

Table 2.1: PMSM Parameters

| Parameter | Symbol | Value | Unit | Parameter | Symbol | Value | Unit |
|---|---|---|---|---|---|---|---|
| Power | $P_n$ | 9200 | [W] | Speed | $n_n$ | 7000 | [rpm] |
| Voltage | $V_n$ | 350 | [V] | Nr. pole pairs | $n_{pp}$ | 1 | [-] |
| Current | $I_{max}$ | 21.31 | [A] | PM flux linkage | $\psi_{pm}$ | 0.53 | [Wb] |
| Torque | $T_n$ | 12.55 | [Nm] | Stator resistance | $R_s$ | 0.05 | [Ω] |
| Inertia | $J$ | 0.008 | $[Kgm^2]$ | Stator inductance | $L_s$ | 25 | [mH] |

Under the assumption that the three phase system is balanced and that the stator resistance and inductance for each phase are equal, the equivalent electrical circuit model of the PMSM can be build and it is shown in Figure 2.3.

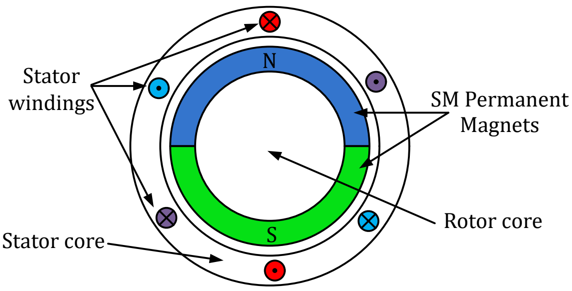


Figure 2.2: Cross section view

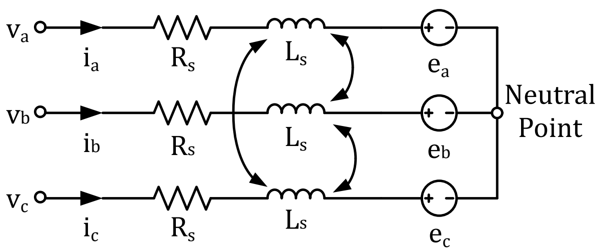


Figure 2.3: Equivalent electrical circuit

Based on Figure 2.3, the governing voltage equations of the machine can be derived.

$$\begin{bmatrix} v_a \\ v_b \\ v_c \end{bmatrix} = \begin{bmatrix} R_s & 0 & 0 \\ 0 & R_s & 0 \\ 0 & 0 & R_s \end{bmatrix} \begin{bmatrix} i_a \\ i_b \\ i_c \end{bmatrix} + \frac{d}{dt} \begin{bmatrix} L_s & 0 & 0 \\ 0 & L_s & 0 \\ 0 & 0 & L_s \end{bmatrix} \begin{bmatrix} i_a \\ i_b \\ i_c \end{bmatrix} + \begin{bmatrix} e_a \\ e_b \\ e_c \end{bmatrix} \tag{2.1}$$

where $v_{a,b,c}$ represent the stator voltages, $i_{a,b,c}$ represent the stator phase currents, $R_s$ is the stator resistance, $L_s$ is the stator inductance and the back electromotive forces are defined as $e_{a,b,c}$. The stationary frame model described by Equation 2.1 is quite complex due to the variation of the stator inductance with respect to the rotor position. In order to simplify the model, the Park and Clarke transformations are being employed, thus transforming the *abc* variables into $dq0$ rotating reference frame. Since the three phase system is considered balanced the zero component will be null. The step-by-step development of the $dq0$ model of the PMSM can be found throughout the literature, but since this is not the main objective of this project, only the final set of equations will be shown:

$$v_d = R_s i_d + L_d \frac{di_d}{dt} - \omega \psi_q \tag{2.2}$$

$$v_q = R_s i_q + L_q \frac{di_q}{dt} + \omega \psi_d \tag{2.3}$$

where,

$$\psi_d = L_d i_d + \psi_{pm} \tag{2.4}$$

$$\psi_q = L_q i_q \tag{2.5}$$

Taking into consideration that a surface mounted permanent magnet machine is being used and that the d- and q-axis inductances are equal ($L_d = L_q$), the electromagnetic torque equation can be expressed as:

$$T_e = \frac{3}{2} n_{pp} \psi_{pm} i_q \tag{2.6}$$

Finally, the mechanical equation of the machine can be defined as:

$$J \frac{d\omega_m}{dt} = T_e - T_{load} - B\omega_m \tag{2.7}$$

This set of 6 equations (Equation 2.2 - Equation 2.7) will be used in order to build the mathematical model of the PMSM and will be implemented in MATLAB/Simulink.

The equivalent electrical circuit representing the dynamic behaviour of the PMSM shown in Figure 2.3, can be redrawn according to the new stator voltage equations, as shown in Figure 2.4 and Figure 2.5.

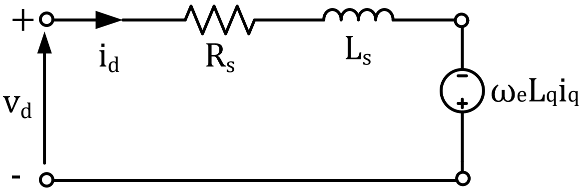


Figure 2.4: d-axis equivalent circuit

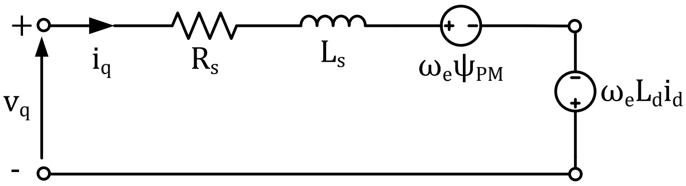


Figure 2.5: q-axis equivalent circuit

### 2.1.1 Field Oriented Control

In order to be able to drive the PMSM, the speed and torque of the machine should be controlled. This can be easily achieved by implementing a proper control strategy. Two of the most common control strategies used in motor drive applications are Field Oriented Control (FOC) and Direct Torque Control (DTC). Even though both methods are able to accurately control the torque of the machine, they have different operating principles, each with its own advantages and disadvantages.

Although DTC has a faster dynamic response, because it does not require any PI controllers or reference frame transformations, the flux and torque hysteresis controllers have a variable switching frequency, which will result in higher switching losses and high current ripple. On the other hand, FOC has a constant switching frequency and is subject to lower current ripple and distortion. [10]

Based on these facts and taking into consideration that the machine can be controlled over the full speed range with good overall dynamic performance, FOC is considered to be the optimum control strategy for this given application.

The general block diagram is shown in Figure 2.6, followed by a brief description of FOC's operating principle. It should be noted that for simplicity reasons, the position of the rotor is measured by an encoder, thus eliminating the need for an estimator block.

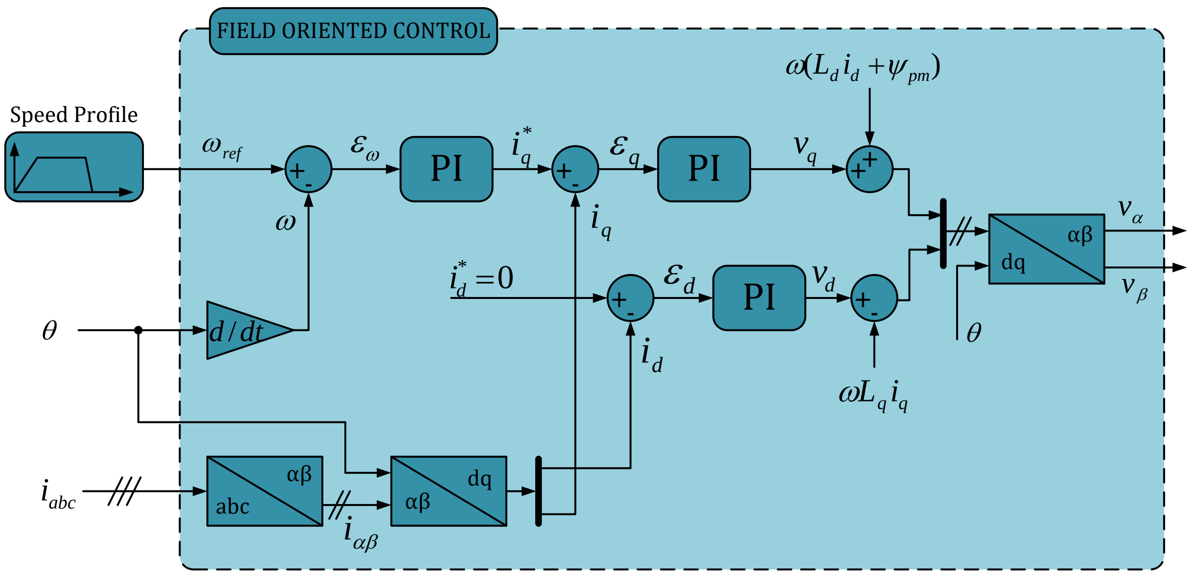


Figure 2.6: Field oriented control block diagram

From Equation 2.6 it is clear that in order to control the torque of the machine, the quadrature axis current $i_q$ should be regulated. Therefore, the measured stator currents $i_{abc}$ must go through the Clarke and Park transformation blocks, so that the resulting d- and q-axis currents $i_{dq}$ can be compared with the given current reference values $i^*_{dq}$.

Here, it should be noted that in order to achieve the maximum torque per amp ratio, it is recommended that all the currents should be on the quadrature axis, thus setting the d-axis current reference $i^*_d$ to 0.

The errors obtained after the above mentioned current comparison are then fed into a d-axis PI current controller, respectively a q-axis PI current controller. Both controllers will try to reduce the current error to 0, by generating corresponding DC voltages $v_{dq}$. After removing the cross-coupling terms, the d- and q-axis voltages go through an inverse Clarke transformation, and the resulting stationary reference frame voltages $v_{\alpha\beta}$ will represent the inputs to the modulation technique block. Finally, based on the magnitude and frequency of the input voltages, the modulation technique block will compute the switching sequence of the active devices of the power inverter, hence closing the inner loop.

The outer control loop is responsible for adjusting the speed of the PMSM. This is done by measuring the actual speed of the machine and comparing it to a speed reference value $\omega_{ref}$. Similar to the current loop, the speed error will be fed into a PI controller, which will output the necessary current reference value $i_q^*$ for eliminating the error.

### 2.1.2 PI Controller Design

As it can be seen in Figure 2.6, three PI controllers are being used within the employed motor control strategy. Two of them are resposible for regulating the d- and q-axis currents and form together the inner control loop and the third PI controller is placed on the outer speed loop.

Due to the fact that $L_d$ is equal to $L_q$, the design of the current regulators will be similar, thus only the q-axis controller will be shown. Before beginning the controller design procedure, the following design requirements are imposed:

- Current overshoot should be less than 5%.
- Speed overshoot should be less than 25%.
- Current loop should be at least 10 times faster than the speed loop.

#### Current PI Controller

The plant transfer function of the current control loop can be derived from the Laplace domain equation of the q-axis voltage (Equation 2.3). In order to have a linear controller, the back EMF term can be treated as a disturbance and be compensated out through decoupling. After removing the cross-coupling term, the plant transfer function ca be expressed as follows:

$$G_{iq}(s) = \frac{i_q(s)}{v_q(s)} = \frac{1}{R_s + sL_s} \tag{2.8}$$

Furthermore, some additional delays need to be inserted within the control loop, so that the continuous time domain system can resemble to the real-life one. The delay added by the *Control Delay* block represents the digital calculation which takes place in the DSP/dSpace. The *PWM Delay* introduces the modulation technique delay, while the *Sampling Delay* block stands for the analog to digital conversion which appears during the current measurement [11].

All the above mentioned delays are introduced as simple first order systems, and therefore, the $i_q$ current control loop can be drawn as shown in Figure 2.7.

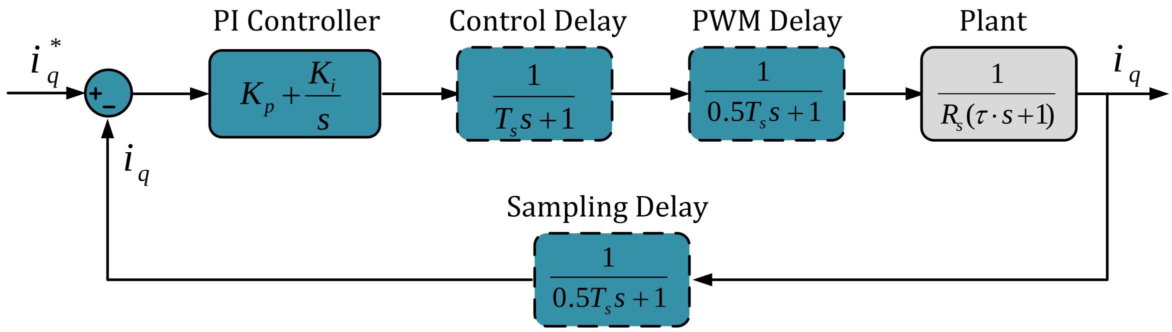


Figure 2.7: $i_q$ current control loop

where, $\tau$ represents the electrical time constant of the plant.

$$\tau = \frac{L_q}{R_s} = \frac{0.025}{0.5} = 0.5[s] \tag{2.9}$$

Since the sampling frequency $f_s$ is considered equal to the switching frequency $f_{sw}$, the sampling period can be calculated as:

$$T_s = \frac{1}{f_s} = \frac{1}{f_{sw}} = \frac{1}{16000} = 0.0625[ms] \tag{2.10}$$

The $i_q$ current loop shown in Figure 2.7 can be further simplified in order to obtain a unity feedback loop as shown in Figure 2.8.

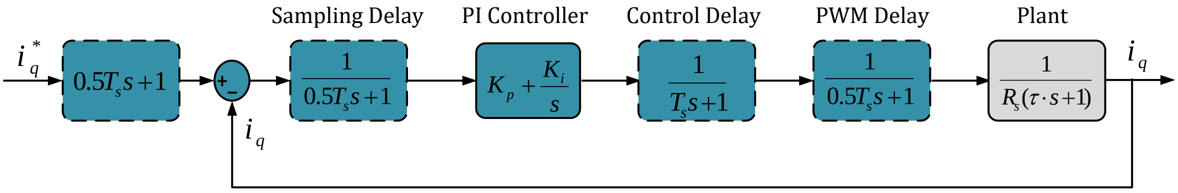


Figure 2.8: $i_q$ Current loop with unity feedback

The time constants of the delays introduced in the system can be added together, hence obtaining an equivalent time constant:

$$T_{eq} = 0.5T_s + 1.5T_s + 0.5T_s = 2T_s = 0.125[ms] \tag{2.11}$$

Therefore, the open loop transfer function of the current control loop can be written as:

$$G_{ol}(s) = \frac{K_p s + K_i}{s} \cdot \frac{1}{T_{eq}s + 1} \cdot \frac{1}{R_s(\tau + 1)} \tag{2.12}$$

By using the Optimal Modulus (OM) criterion, the zero of the PI transfer function can be used to eliminate the slowest pole, thus increasing the dynamics of the system [12]. Therefore:

$$\tau_{PI} = \tau \Rightarrow \frac{K_p}{K_i} = \frac{L_q}{R_s} \tag{2.13}$$

After canceling-out the slowest pole of the system, the open loop transfer function shown in Equation 2.12 can be re-written as follows:

$$G_{ol}(s) = \frac{K_p}{s\tau_{PI}} \cdot \frac{1}{R_s(T_{eq}s + 1)} \tag{2.14}$$

Optimal Modulus criterion states that the general transfer function of a second order system with a damping factor of $\zeta = 0.707$ can be expressed as in Equation 2.15 [12].

$$G_{OM}(s) = \frac{1}{2\tau s(\tau s + 1)} \tag{2.15}$$

The proportional gain of the PI controller can be calculated from the equation obtained by comparing the open loop transfer function of the system (Equation 2.12) with the generalized transfer function of a second order system (Equation 2.15).

$$\frac{K_p}{R_s \tau} = \frac{1}{2T_{eq}} \tag{2.16}$$

Hence,

$$K_p = \tau \cdot \frac{R_s}{2T_{eq}} = 0.5 \cdot \frac{0.05}{2 \cdot 0.125 \cdot 10^{-3}} = 100 \tag{2.17}$$

The integral gain of the PI controller can be determined by inserting the PI time constant and the proportional gain value in the PI transfer function.

$$G_{PI}(s) = K_p \cdot \frac{1 + s\tau}{s\tau} = 100 \cdot \frac{1 + s0.5}{s0.5} = \frac{100 + 50s}{0.5s} = \frac{200}{s} + 100 \tag{2.18}$$

The Bode diagram of the open loop system has been plotted in Figure 2.9, and it can be observed that the closed loop system is Stable. The corresponding phase margin is equal to PM = 62.9[deg] and the gain margin GM = 15.2[dB], while the bandwidth of the current control loop is equal to 609.56[$Hz$].

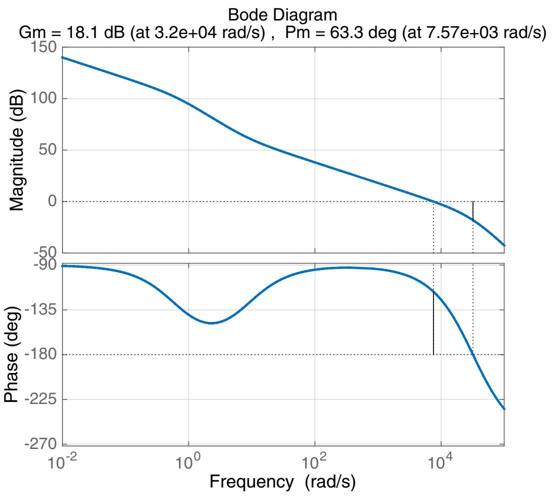


Figure 2.9: Bode diagram - $i_q$ control loop

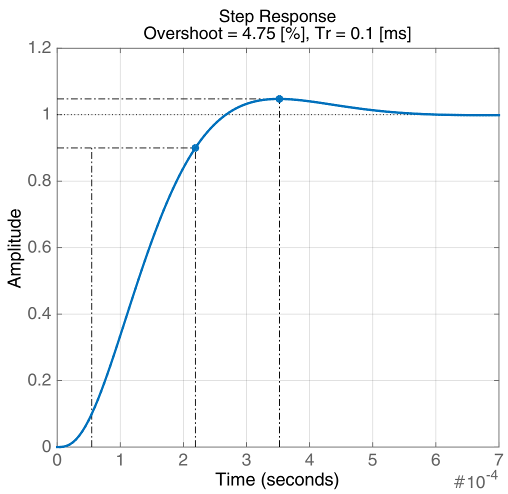


Figure 2.10: Step response - $i_q$ control loop

Furthermore, from the step response of the closed loop system, which can be seen in Figure 2.10, the rise time ($T_r = 0.31[ms]$) and the settling time ($T_{settling} = 0.9[ms]$) can be identified. Additionally, it can be noticed that the $i_q$ current response has an overshoot of 4.61%, which is within the required design limits.

Finally, for simplicity reasons, the equivalent transfer function of the current control closet loop system, which will be used during the design of the outer speed loop, can be approximated as a first order system with a time constant of $T_{crt} = 0.31[ms]$, and can be written as:

$$G_{crt}(s) = \frac{i_q(s)}{i_q^*(s)} = \frac{1}{T_{crt}s + 1} = \frac{1}{0.00031s + 1} \tag{2.19}$$

### Speed PI Controller

Unlike the current loop, where the plant transfer function was obtained from the voltage equation of the machine, for the speed loop, the plant transfer function can be derived from the mechanical equation. If the viscous friction $B_m$ is neglected the plant transfer function can be defined as:

$$\frac{\omega_e(s)}{T_e(s) - T_{load}(s)} = \frac{n_{pp}}{Js} \tag{2.20}$$

In a similar manner to the current loop design, some delays need to be introduced in the system so that it can resemble to the real life model [11].

From the speed loop design, shown in Figure 2.11, it can be noticed that the system has 2 inputs: the load torque $T_{load}$ and the reference speed $\omega_{ref}$. Therefore, the system can be considered linear, and the superposition principle can be applied, resulting in 2 cases. In the first case, the reference speed is considered as an input and the load torque can be seen as a disturbance and it can be set to 0, while in the second case the load torque is seen as an input and the reference speed can be viewed as a disturbance [13].

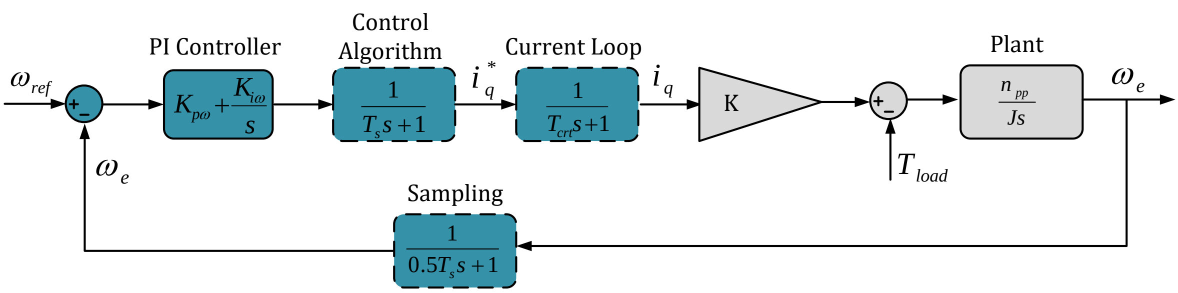


Figure 2.11: Speed control loop

Since this is not the main purpose of this project and for simplicity reasons, only the first case scenario will be taken into consideration. Hence, the reference speed will be the only input to our system and the load torque will be neglected. The new model diagram can be further simplified by introducing a unity gain feedback. The speed loop design can be seen in Figure 2.12.

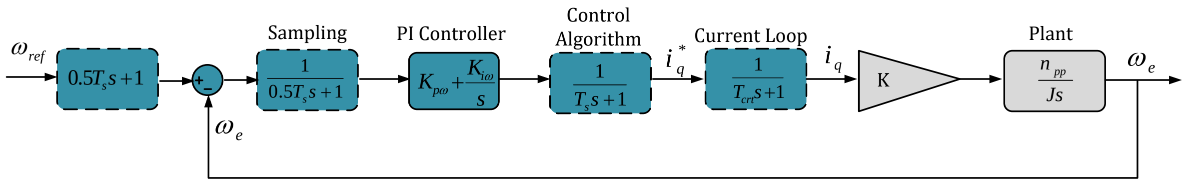


Figure 2.12: Speed loop with unity gain feedback

After adding together all the time constants introduced by the different delays of the system $T_{eq_\omega} = 0.5T_s + T_s + T_{crt} = 0.403[ms]$, the equivalent time constant can be introduced in the open loop transfer function of the system, shown in Equation 2.21.

$$G_{ol_\omega}(s) = K_{p_\omega} \cdot \frac{1}{(T_{eq_\omega}s+1)} \cdot K \cdot \frac{n_{pp}}{Js} \tag{2.21}$$

where,

$$K = \frac{3}{2} n_{pp} \psi_{pm} \tag{2.22}$$

Again, by applying the *Optimal Modulus* criterion, and comparing the generic transfer function of a second order system with the open loop transfer function of the speed loop, the following equation can be derived:

$$\frac{K_{p_\omega}}{J} K n_{pp} = \frac{1}{2T_{eq_\omega}} \tag{2.23}$$

Thus, the proportional gain can be calculated:

$$K_{p_\omega} = \frac{J}{2T_{eq_\omega} K n_{pp}} = \frac{0.008}{2 \cdot 0.401 \cdot 10^{-3} \cdot 1.5 \cdot 0.53} = 12.778 \tag{2.24}$$

In order to find the value of the integral gain of the controller, the *Symmetry Optimum* criterion can be applied, to approximate the value of the time constant of the PI controller [14].

$$\tau_\omega = 4T_{s_\omega} = 4 \cdot 0.401 = 1.604[ms] \tag{2.25}$$

After introducing the values of the proportional gain and time constant, the PI transfer function can be expressed as:

$$G_{PI_\omega}(s) = 12.778 \cdot \frac{1+s0.0016}{s0.0016} = \frac{12.77+s0.0204}{s0.0016} = \frac{7918.25}{s} + 12.77 \tag{2.26}$$

From the Bode diagram of the open loop system (shown in Figure 2.13), it can be noticed that, even though the closed loop system appears to be stable, the bandwidth of the speed loop is equal to $206.9[Hz]$. Thus, the system is too fast, and does not meet the requirements imposed at the begging of the controller design procedure. Similarly, from the step response of the closed loop system presented in Figure 2.14, an overshoot of 49.2% can be observed, which again, does not meet the limit requirements.

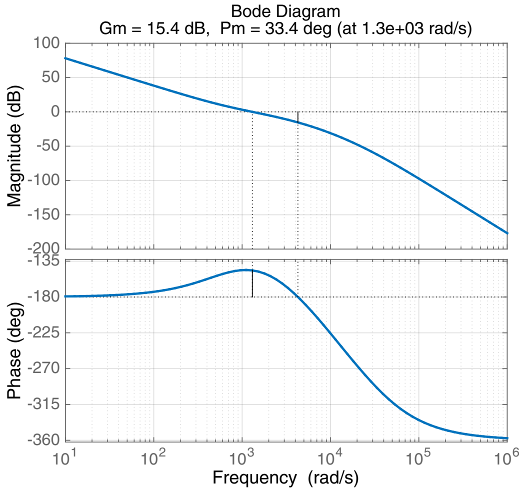


FIGURE 2.13: Bode diagram - $\omega_e$ control loop

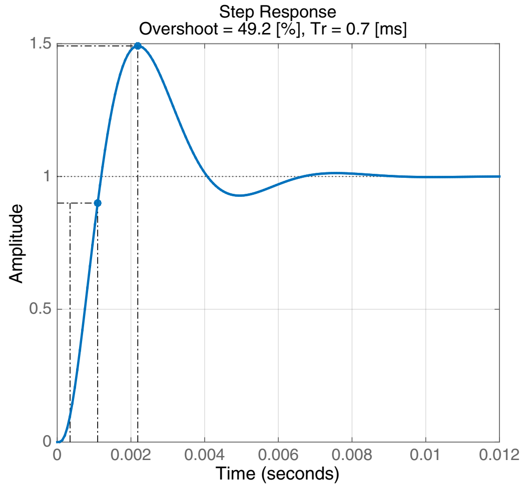


FIGURE 2.14: Step response - $\omega_e$ control loop

Therefore, after proper tuning, the following PI controller gains are obtained: $K_p = 1.277$ and $K_i = 32.453$. By plotting the Bode diagram of the open loop system with the new PI values (Figure 2.15) , it can be noticed that the system is slower, having a bandwidth of $20.53[Hz]$, which is approximately 30 times slower than the current loop. Besides that, the system remains stable, with a phase margin of $PM = 75.7[deg]$ and a gain margin of $GM = 37.8[dB]$.

Additionally, from the step response of the closed loop system (plotted in Figure 2.16), it can be observed that the speed response has an overshoot of 12% and a rise time of $T_r = 11.5[ms]$. The speed controller now meets all the requirements set at the beginning of the design procedure.

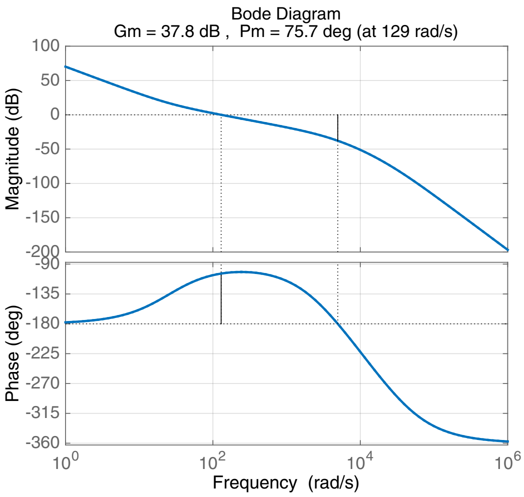


FIGURE 2.15: Bode diagram - $\omega_e$ control loop

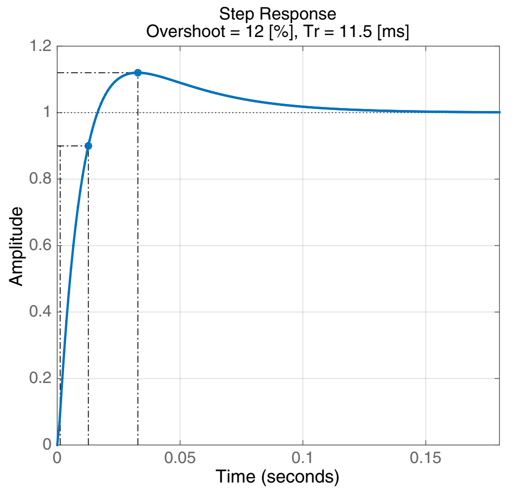


FIGURE 2.16: Step response - $\omega_e$ control loop

### Anti-Windup

Because of the current and voltage limitations set by the physical system, the PI controllers need to be implemented with an anti-windup. If the output current/voltage demand of the controller reaches the upper saturation limit, an anti-windup based on the *Back Calculation* method is used in order to reduce the internal integrator of the PI. The block diagram of the controller with a *Back Calculation* anti-windup in shown in Figure 2.17.

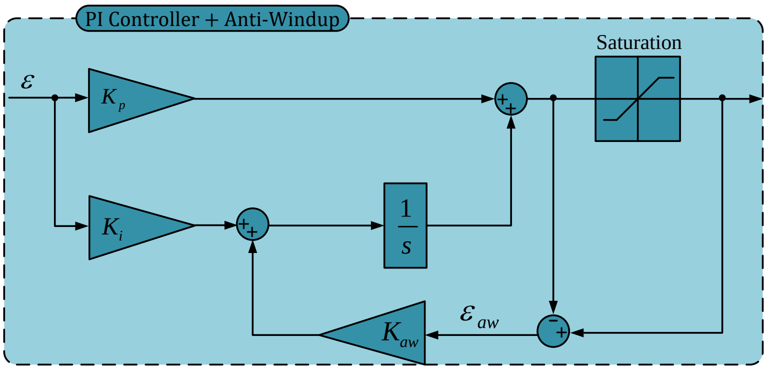


Figure 2.17: PI regulator with anti-windup

The tracking constant, for the current and speed controllers, $K_{aw}$ placed on the saturation feedback loop is usually determined according to the following formulas:

$$K_{aw_i} = 0.1 \cdot \frac{K_{p_i}}{K_{i_i}} = 0.1 \cdot \frac{100}{200} = 0.05 \tag{2.27}$$

$$K_{aw_\omega} = 0.1 \cdot \frac{K_{p_\omega}}{K_{i_\omega}} = 0.1 \cdot \frac{1.277}{32.453} = 0.003 \tag{2.28}$$

## 2.2 Voltage Source Inverter

As previously mentioned, a Voltage Source Inverter (VSI) is used in order to drive the PMSM. The topology of a two level three phase inverter can be seen in Figure 2.18. The VSI is composed of 6 semiconductor devices (switches) which under a given ON/OFF state will provide a voltage equal to $V_{dc}$ or $-V_{dc}$ at the output terminals of the inverter, hence the two voltage levels.

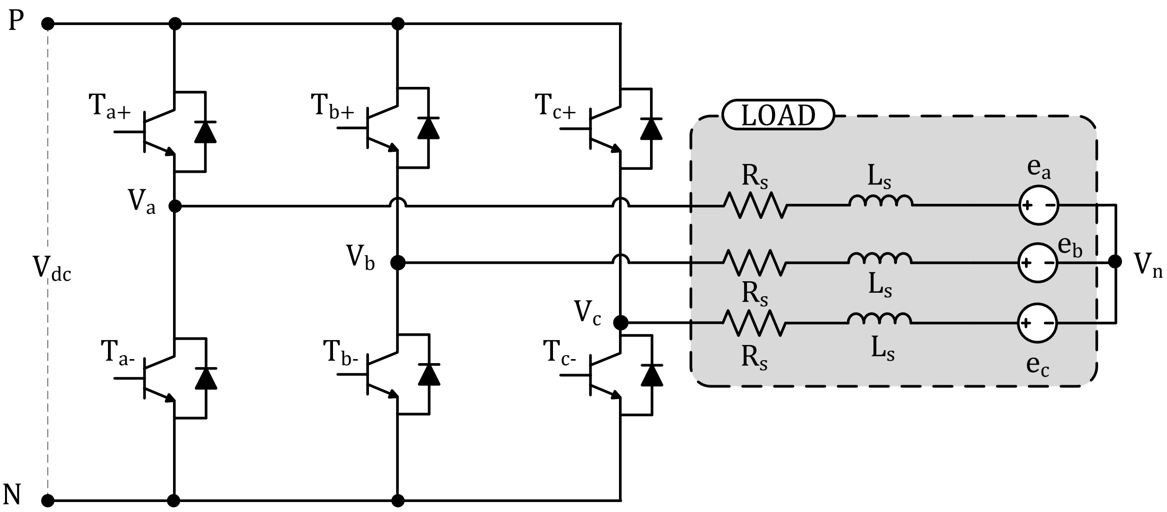


Figure 2.18: Three phase VSI

The VSI can be mathematically modelled by expressing the output phase-to-neutral voltage as a function of the DC voltage and the switching states of the power devices. Therefore, based on Figure 2.18, the phase-to-neutral voltage can be initially defined as:

$$\begin{bmatrix} V_{an} \\ V_{bn} \\ V_{cn} \end{bmatrix} = \begin{bmatrix} V_{aN} - V_{nN} \\ V_{bN} - V_{nN} \\ V_{cN} - V_{nN} \end{bmatrix} \tag{2.29}$$

Assuming that the load in symmetric and balanced,

$$V_{an} + V_{bn} + V_{cn} = 0 \tag{2.30}$$

the $V_{aN}$, $V_{bN}$ and $V_{cN}$ voltages can be determined based on their switching states $S_{abc}$.

$$\begin{bmatrix} V_{aN} \\ V_{bN} \\ V_{cN} \end{bmatrix} = V_{dc} \begin{bmatrix} S_a \\ S_b \\ S_c \end{bmatrix} \tag{2.31}$$

By manipulating Equation 2.29 and Equation 2.30, the phase-to-neutral voltages of the inverter can be expressed as follows:

$$\begin{bmatrix} V_{an} \\ V_{bn} \\ V_{cn} \end{bmatrix} = \frac{1}{3} \begin{bmatrix} 2V_{aN} - V_{bN} - V_{cN} \\ -V_{aN} + 2V_{bN} - V_{cN} \\ -V_{aN} - V_{bN} + 2V_{cN} \end{bmatrix} \tag{2.32}$$

Finally, by substituting Equation 2.31 into Equation 2.32, the mathematical model of the two level inverter can be derived:

$$\begin{bmatrix} V_{an} \\ V_{bn} \\ V_{cn} \end{bmatrix} = \frac{V_{dc}}{3} \begin{bmatrix} 2 & -1 & -1 \\ -1 & 2 & -1 \\ -1 & -1 & 2 \end{bmatrix} \begin{bmatrix} S_a \\ S_b \\ S_c \end{bmatrix} \tag{2.33}$$

### 2.2.1 Discontinuous Pulse Width Modulation

In order to control the speed of the motor, the VSI must supply a variable frequency and amplitude voltage at the terminals of the PMSM. This can be achieved by means of Pulse Width Modulation (PWM), which will generate a binary sequence signal (1 - ON, 0 - OFF) for the active semiconductor devices, based on a reference voltage. There are numerous PWM techniques which can fulfill the aforementioned task, each with its own advantages and disadvantages. Even though continuous PWM techniques such as Sinusoidal PWM (SPWM) or Space Vector Modulation (SVM) have a low harmonic distortion, the use of a Discontinuous PWM (DPWM) strategy will significantly reduce the switching losses [15]. Furthermore, in [16]-[17], it has been shown that by using the DPWM1 technique, the thermal cycles which occur in the power devices will be reduced. Therefore, the modulation technique choice for the this thesis will be DPWM1.

This particular modulation strategy is also known as $60^o$ - flat top technique, due to the fact that for $60^o$ the modulation wave will be clamped. Hence, during that interval, no modulation will occur, which means that there will be no switching losses.

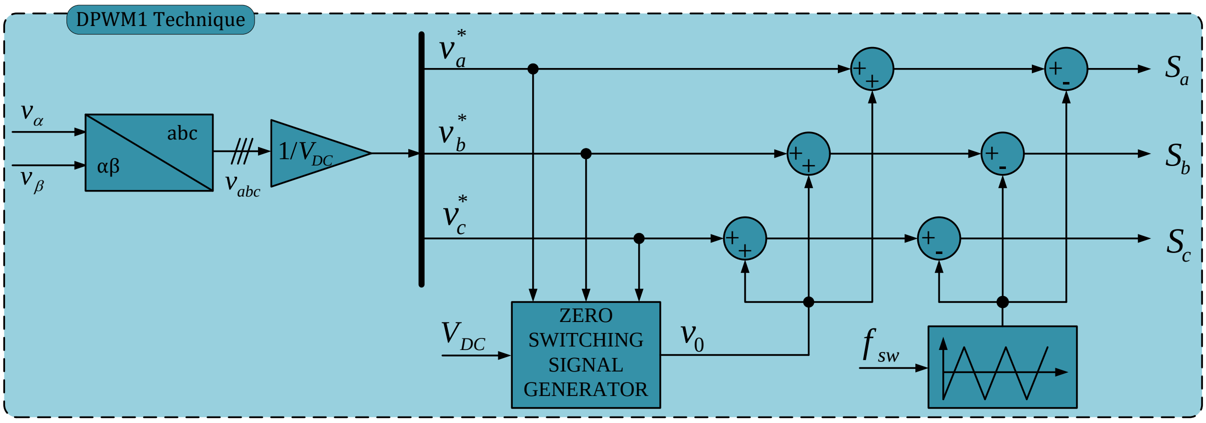


Figure 2.19: DPWM1 technique

As illustrated in Figure 2.19, the control voltage signal is obtained by adding a zero sequence signal ($v_0$) to the sinusoidal voltage references ($v_{abc}^*$). Assuming that,

$$|v_a^*| \geq |v_b^*|, |v_c^*|$$

the zero sequence voltage can be determined by using the following formula [15]:

$$v_0 = (\text{sign}(v_a^*))\frac{V_{dc}}{2} - v_a^* \tag{2.34}$$

The resulting zero sequence signal and control voltage can be seen in Figure 2.21, respectively Figure 2.21.

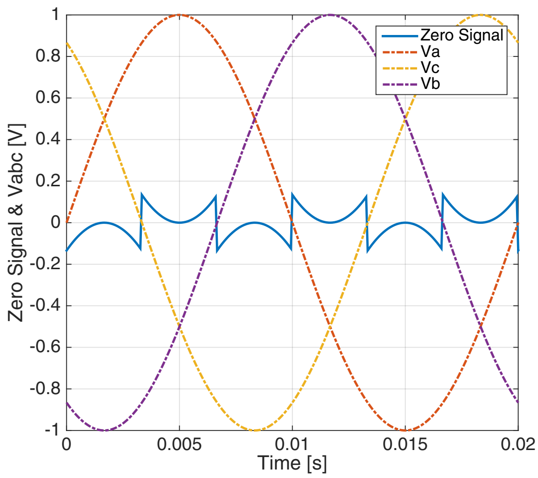


Figure 2.20: Zero sequence signal

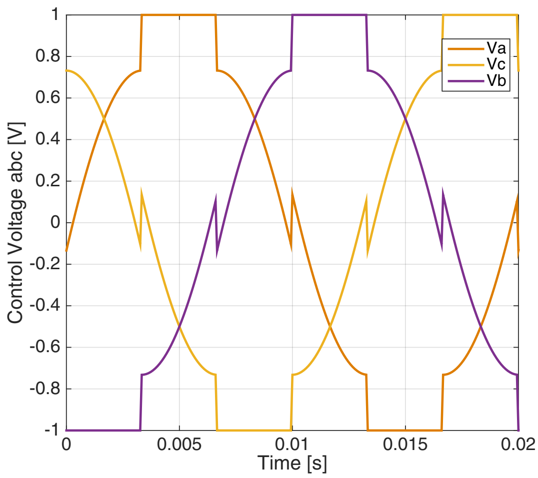


Figure 2.21: Control voltage

## 2.3 Power Loss Model

It is well known that the power losses which occur in semiconductor devices include conduction losses, switching losses and blocking losses. Due to their insignificant impact of the total power losses, the blocking losses can be neglected. Therefore:

$$P_{\text{device}} = P_{\text{cond}} + P_{\text{sw}} \tag{2.35}$$

Conduction losses appear during the period in which current is flowing through the device, thus resulting in power dissipation due to the internal on-state resistance of the power device. Similarly, switching losses are caused by the power dissipated during the period of time in which the device switches from one state to another. In order to correctly identify and analyze the factors which influence the power device losses, the switching characteristics of a power diode and an IGBT, will be given, as presented in [1].

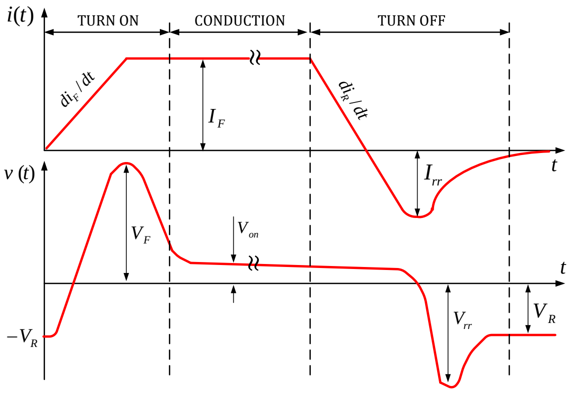


Figure 2.22: Diode switching characteristic

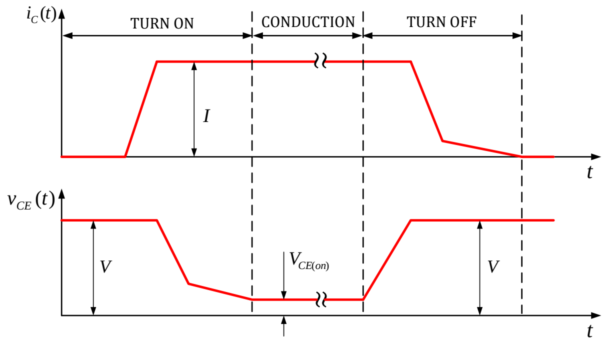


Figure 2.23: IGBT switching characteristic

As it can be seen from the diode switching waveform, shown in Figure 2.22, almost all power losses occur when the diode is forward bias. In that period of the time, the diode is in conduction, thus current ($I_F$) will be flowing through the diode and the on-state voltage drop ($V_{on}$) will appear across its terminals. Additionally, during the turn on process, a high voltage overshoot appears when the reserve bias voltage of the diode is removed. According to [1], the voltage overshoot is dependent of the current time rate of change $di_F/dt$ and the electrical circuit in which the diode is being used. Similarly, when the diode switches from conduction to blocking state, the stored charge of the diode, will discharge with the rate $di_R/dt$. The total amount of time required by the diode to recover is know as reverse recovery time, and in this time period the diode will conduct the reverse recovery current ($I_{rr}$) in reverse direction, thus generating power losses.

From the IGBT switching characteristic, presented in Figure 2.23, it can be observed that, similarly to the power diode, the main period of time during which the IGBT will generate losses is when it is conducting. This is due to the load current ($I$) which is flowing through the collector. By looking at the turn-on state, it can be seen that the voltage drop across the transistor remains at the voltage level ($V$) until the collector current ($i_C$) reaches the load current value. Once $i_C = I$, the collector-emitter voltage ($v_{CE}$) will start to decrease until it reaches its on-state value ($V_{CE(on)}$). During this transition, both the current and the voltage are positive and will produce losses, know as turn-on losses. The transient behaviour of the IGBT when switched off is quite similar to the turn-on, with the difference that the turn-off required time is longer. This is due to the stored charge in the $n^-$ drift region of the IGBT, which will lead to the "tailing" of the collector current [1]. The presence of the collector current, together with the fact that the $v_{CE}$ voltage is at its off-state value will result in additional power losses.

Based on these facts, it can be concluded that the conduction losses which occur in power semiconductor devices are mainly dependent on the conduction voltage of the device and the load current, while the switching losses are determined by the switching frequency and the switching energy of the device.

### 2.3.1 Conduction Losses

With respect to the load current input $i_{abc}$, received from the *Motor Drive Model* the average switching cycle conduction losses of the transistor/diode can be calculated with the following function:

$$P_{\text{cond@}T_L/T_H} = V_{\text{cond@}T_L/T_H}(i_{abc}) \cdot i_{abc} \cdot d_{abc} \tag{2.36}$$

where, $V_{\text{cond@}T_L/T_H}$ represents the conduction voltage of the device at a given low temperature ($T_L$) or high temperature ($T_H$) reference, while $d_{abc}$ represents the duty ratio. Usually, the conduction voltage value is given in the device datasheet, but in case it not available, it can be determined through simple curve fitting, by means of the following function:

$$V_{\text{cond@}T_L/T_H}(i_{abc}) = V_{\text{cond0@}T_L/T_H} + (i_{abc})^{B_{\text{cond@}T_L/T_H}} \tag{2.37}$$

In this thesis, the above mentioned equation will be used in order to fit, the conduction voltage curve which was empirically found in a previous project. At this point it should be noted that, in order to correlate to the available experimental setup which consists of a three level Neutral Point Clamped (NPC) inverter, the transistor power losses will be calculated for the upper MOSFET switch of the laboratory converter. Since, the power devices are considered ideal in the simulation model, this will have no influence on the motor drive behaviour.

The conduction voltage curves at low and high temperature references of the power diode and MOSFET, are shown in Figure 2.24, respectively Figure 2.25.

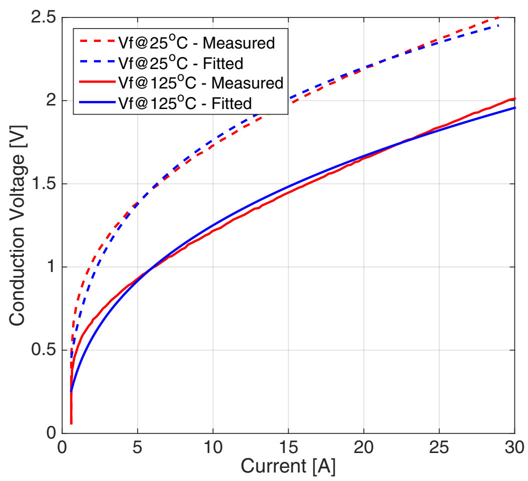


Figure 2.24: Diode forward voltage curve

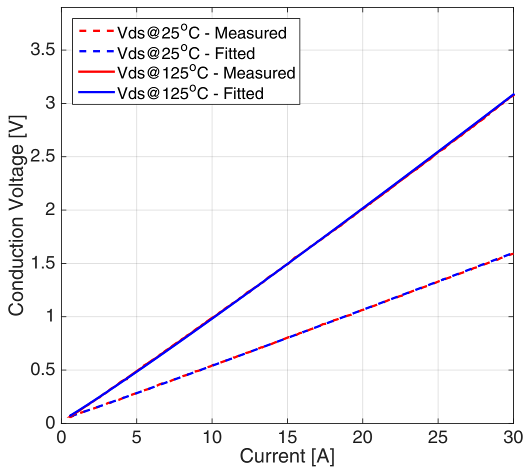


Figure 2.25: MOSFET drain-source voltage curve

The resulting parameters of the curve fitting algorithm will be substituted in Equation 2.37, which will then be introduced in Equation 2.36.

### 2.3.2 Switching Losses

Similarly, based on the switching frequency ($f_{sw}$) of the inverter used in the *Motor Drive Model*, the switching losses at a given low temperature ($T_L$) or high temperature ($T_H$) reference can be computed by means of the following function:

$$P_{\text{sw@}T_L/T_H} = f_{sw} \cdot E_{\text{sw@}T_L/T_H} \tag{2.38}$$

where, $E_{\text{sw@}T_L/T_H}$ represents the switching energy of the device. Hence, for the power diode the reverse recovery energy ($E_{\text{rr@}T_L/T_H}$) will be taken into account, while for the MOSFET the turn-on ($E_{\text{on@}T_L/T_H}$) and turn-off ($E_{\text{off@}T_L/T_H}$) energies. Additionally, because the switching loss function shown in Equation 2.38 does not take into account the advantages of the DPWM1 technique, a logical circuit that will assure that the there will be no switching during the periods in which the DPWM1 modulation wave is clamped has been implemented. If the switching energy values are not provided by the manufacturer, the following function can be used in order to determine it:

$$E_{\text{sw@}T_L/T_H} = \left(\frac{V_{dc}}{V_{test}}\right)^K [S_1(i_{abc})^2 + S_2(i_{abc}) + S_3] \tag{2.39}$$

where, $V_{test}$ represents the test voltage and $K$ presents the scaling factor.

Following the same procedure as for the conduction losses, a curve fitting algorithm has been applied to switching loss curves, which were also obtained in previous project. First, the turn-on and turn-off switching energies of the MOSFET at $25^oC$ and $125^oC$ reference temperatures have been plotted in Figure 2.26 and Figure 2.27.

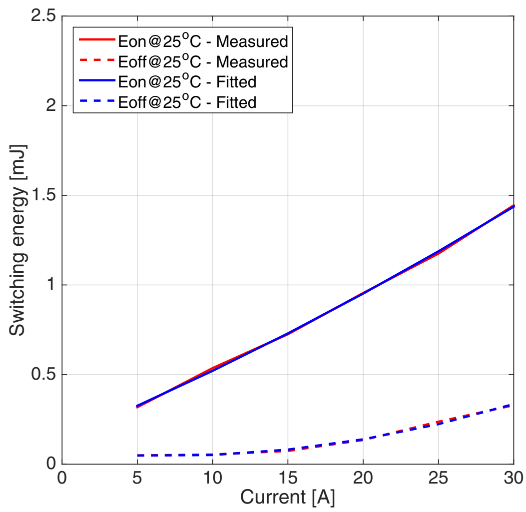


Figure 2.26: MOSFET switching energy at $25^oC$

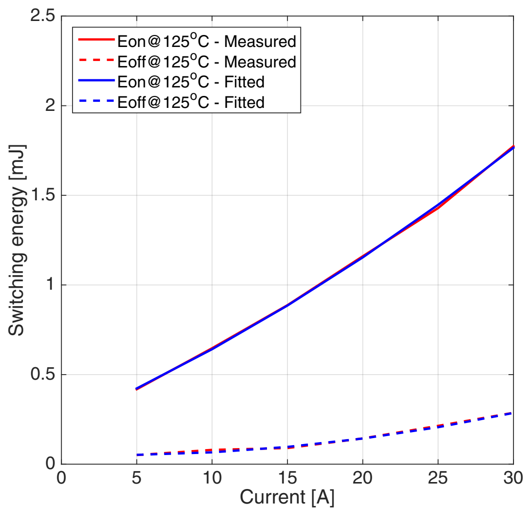


Figure 2.27: MOSFET switching energy at $125^oC$

By adding together the turn-on and turn-off switching energies, the total switching energy which occurs in the MOSFET can be determined, as show in Figure 2.29. The reverse recovery energy curve of the power diode is presented in Figure 2.28.

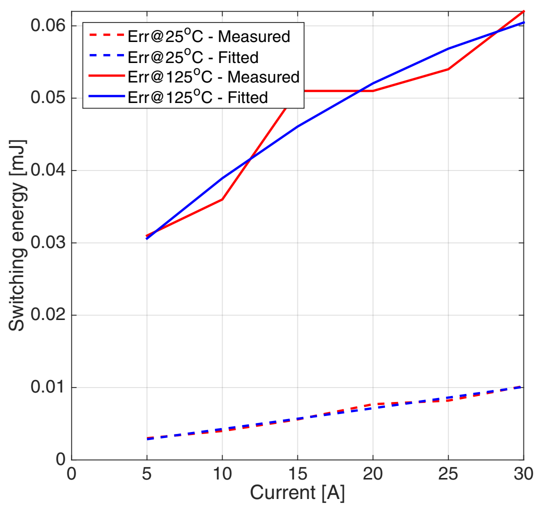


Figure 2.28: Diode reverse recovery curve

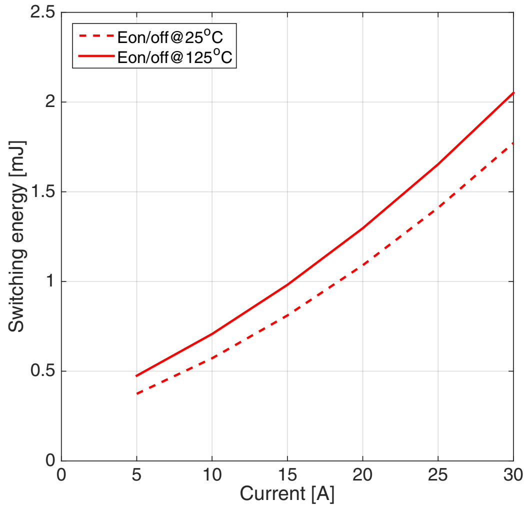


Figure 2.29: MOSFET On/Off switching energy

Finally, the fitted parameters will be introduced into Equation 2.39, which will represent the input for the instantaneous switching loss function (Equation 2.38).

### 2.3.3 Temperature Dependency

In [18],[19], [20] and [21], the dependency between the junction temperature and the loss characteristics of power semiconductor devices has been emphasized. Therefore, the junction temperature of the transistor or diode can be introduced as a feedback variable from the thermal model. By taking into account the conduction and switching loss functions, together with the low temperature ($T_L$) and high temperature ($T_H$) references, the power loss equation as a function of junction temperature can be written as:

$$P_{\mathrm{sw/con@}T_j} = \frac{P_{\mathrm{sw/con@}T_H} - P_{\mathrm{sw/con@}T_L}}{T_H - T_L}(T_j - T_L) + P_{\mathrm{sw/con@}T_L} \tag{2.40}$$

Furthermore, the total power losses which appear in the power device, initially defined as in Equation 2.35 can be expressed as follows:

$$P_{\mathrm{device@}T_j} = P_{\mathrm{cond@}T_j} + P_{\mathrm{sw@}T_j} \tag{2.41}$$

Finally, the average switching cycle power loss characteristics of the power device can be modelled based on the aforementioned equations. The block diagram of the *Power Loss Model* is shown in Figure 2.30. Besides the fitted device parameters, it is clear that the model is highly dependent on the inputs from the *Motor Drive Model* and *Thermal*, thus assuring that a precise power loss estimation, based on certain motor mission profile inputs.

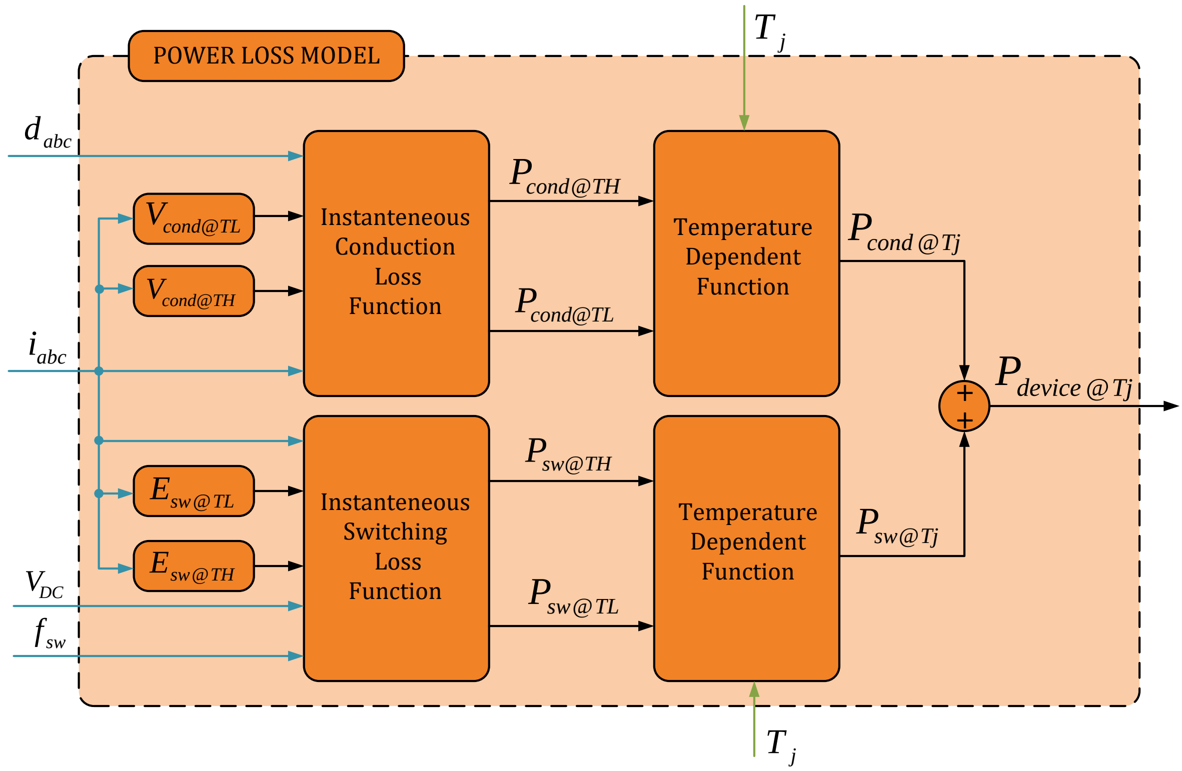


Figure 2.30: Power loss model diagram

It should be noted that, while the Instantaneous Switching Loss Function block is based on Equation 2.38 and the modulation technique, the Instantaneous Conduction Loss Function is solely based on Equation 2.36. The total power device output of the model will be the input to the *Thermal Model*.

## 2.4 Thermal Model

The thermal performance of the power semiconductor devices can be analyzed by means of RC circuit network. Two of the most commonly employed thermal networks are the Foster model and the Cauer model. The Cauer model, also known as ladder network, is based on the actual physical temperature of each layer of the power device (e.g. chip, chip solder, etc.), thus making it extremely difficult to have a precise estimation of its thermal resistance and thermal capacitance values [17], [22].

On the other hand, the parameters involved in modelling the Foster network have no phyisical meaning, and can be either found in the device datasheet or can be derived by experimentally fitting the thermal impedance curve of the device. Therefore, the multilevel Foster network shown in Figure 2.31 will be used in order to translate the power losses of the device to its junction temperature. Moreover, the temperature potential of the case temperature needs to be added to the Foster network for an accurate estimation [23]. As mentioned in the thesis limitations, the case temperature of the semiconductor devices is considered constant, therefore the influence of its dynamical behaviour on the junction temperature will not be analyzed.

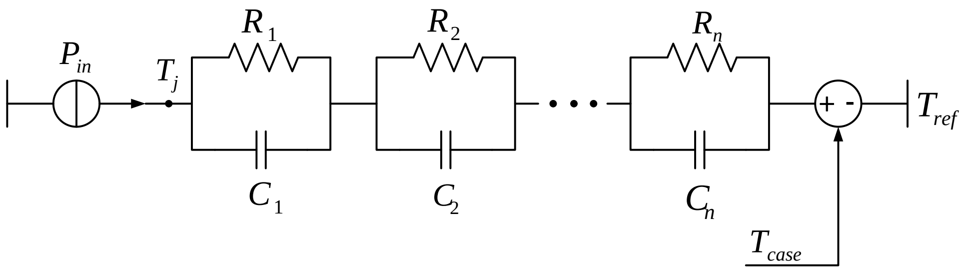


Figure 2.31: Foster RC thermal network

In order to determine the parameters of the Foster thermal network, the following formula has been used to fit the thermal impedance curve of the devices:

$$Z_{\text{th(j-c)}} = \sum_{i=1}^{n} R_i(1 - e^{-\frac{1}{\tau_i}}) \tag{2.42}$$

where, $n$ represents the number of levels of the network and,

$$\tau_i = R_i \cdot C_i \tag{2.43}$$

As it can be seen in Figure 2.32 a three level Foster network can be used to determine the thermal impedance of the diode, while in the case of the power MOSFET, a two level Foster network is sufficient in order to accurately fit the thermal impedance curve, as presented in Figure 2.33.

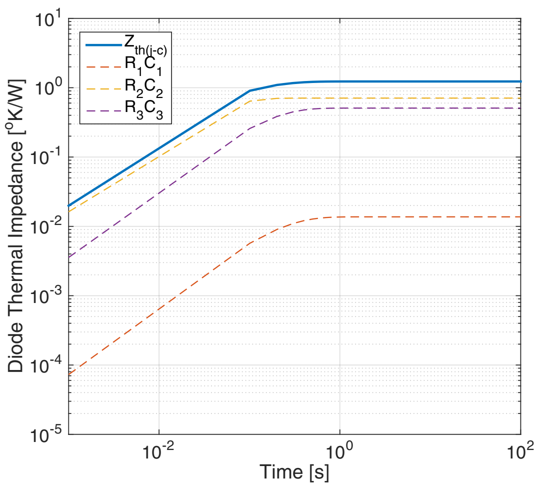


Figure 2.32: Diode thermal impedance

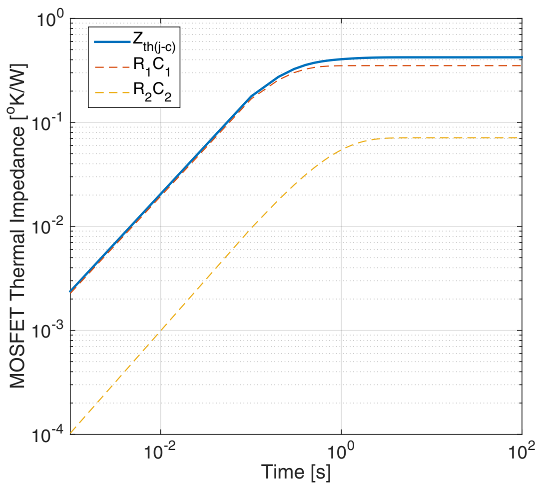


Figure 2.33: MOSFET thermal impedance

Therefore, based on the estimated thermal resistance and capacitance values and on the input power losses generated by the device, the thermal cycling which occurs on the diode or on the transistor can be determined as follows:

$$T_j(t) = P_{in}(t) \cdot Z_{\text{th(j-c)}}(t) + T_{case} \tag{2.44}$$

Finally, by taking into consideration the above mentioned equation, the large signal thermal model of the power devices can be derived from the Foster network. The block diagram of the thermal model is presented in Figure 2.34.

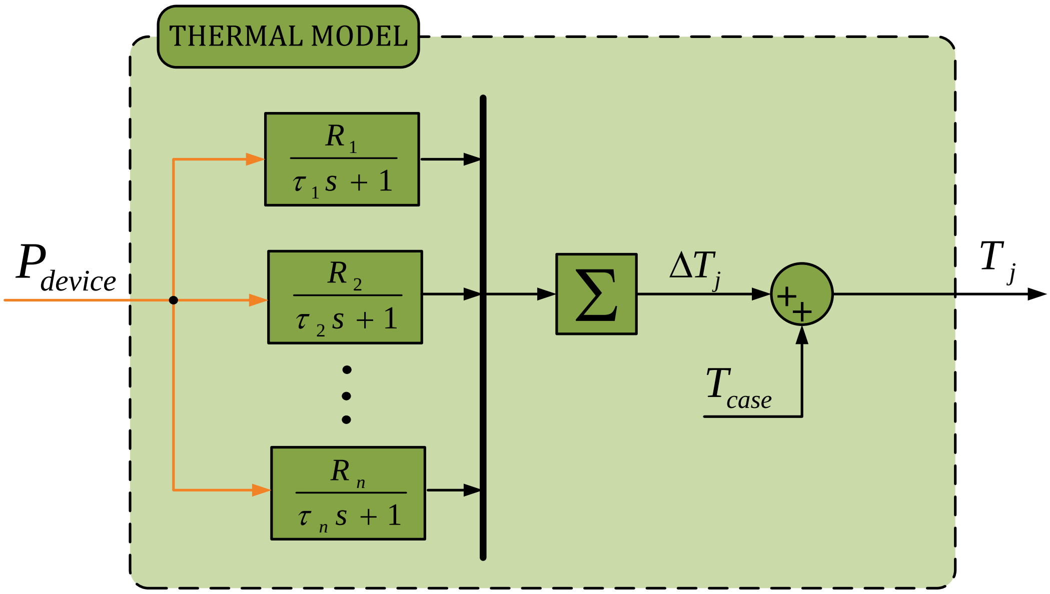


Figure 2.34: Thermal model diagram

## 2.5 Simulation Results

All the models described within this chapter have been implemented in MATLAB/Simulink. In order to reduce the computational time of the simulation, the inverter model has been replaced with a first order system delay. The inputs for the system are the speed and torque mission profiles, which are shown in Figure 2.35 and Figure 2.36.

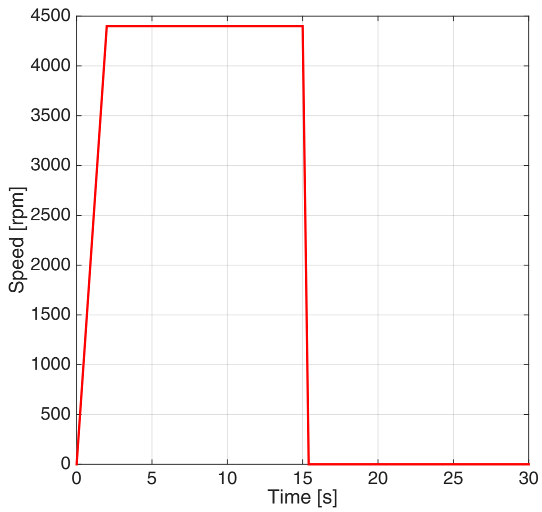


Figure 2.35: Speed mission profile

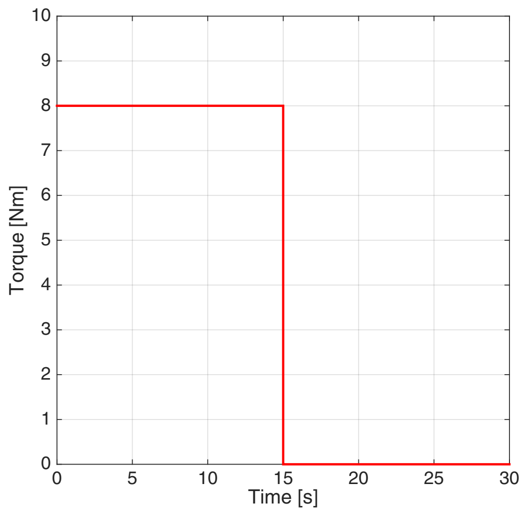


Figure 2.36: Torque mission profile

After modelling the speed profile as the reference speed and the torque profile as the load torque of the PMSM, the simulation is run with a fixed time-step of $T_s = 1/f_{sw} = 0.0625$[ms]. By looking at Figure 2.37, it can be seen that the rotor speed follows accurately the speed profile, while the high current demand which occurs during the acceleration and deceleration periods will cause an overshoot in the electromagnetic torque response of the motor.

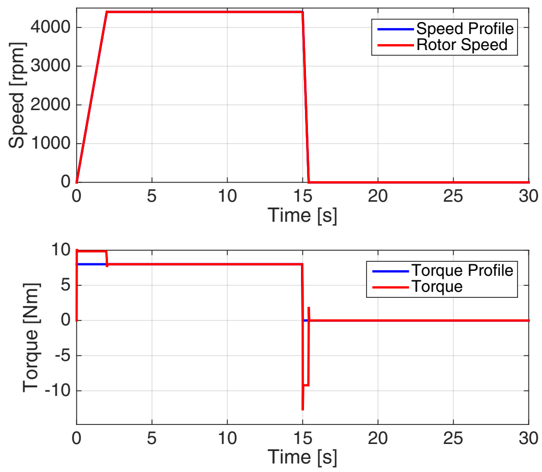


Figure 2.37: Rotor speed & torque of the PMSM

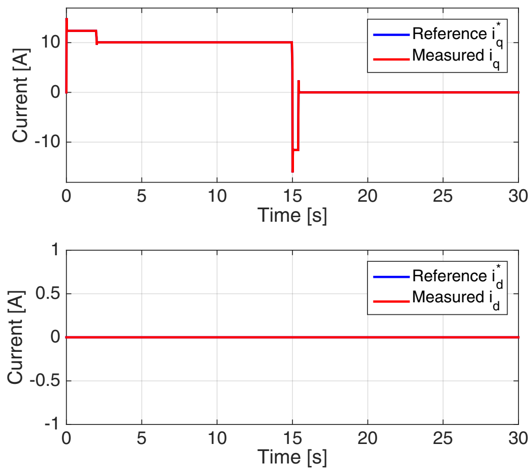


Figure 2.38: $i_q$ & $i_d$ Currents

The response of the *dq* reference frame currents, shown in Figure 2.38, confirm the fact that the PI current regulators have been designed correctly, and that they are able to assure a fast and precise control of the d- and q-axis currents.

Due to the fact that the inverter model has been replaced by a simple delay, the phase voltages of the PMSM will be supplied directly from the modulation technique, proportional with the DC link voltage. Thus, its waveform will correspond to the control voltage waveform of the DPWM1, as presented in Figure 2.39.

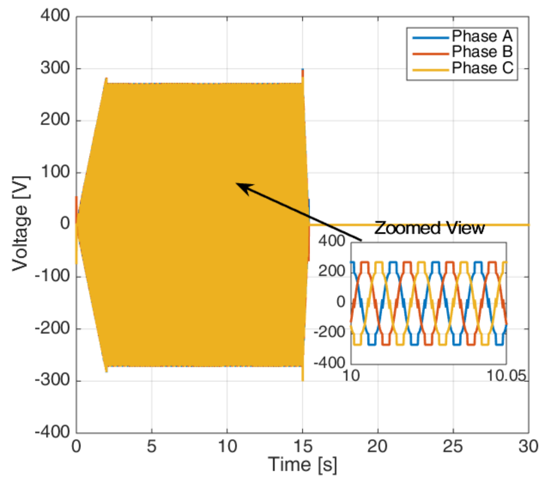


Figure 2.39: Phase voltages

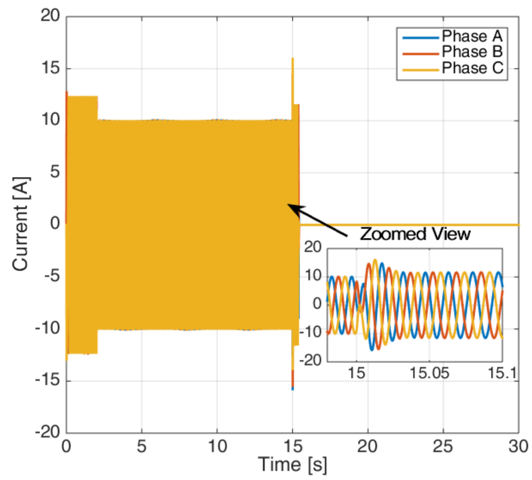


Figure 2.40: Phase currents

As expected, a large amplitude current will be generated during the acceleration and deceleration periods of the motor. Additionally, as shown in the zoomed view figure of the phase currents plot, the current will change its polarity when braking, thus explaining the negative torque overshoot of the PMSM, presented beforehand.

Based on the outputs from the *Motor Drive Model* the average switching cycle power losses which occur in the power semiconductor devices can be determined. Thus, by looking at the conduction and switching losses of the MOSFET and power diode, shown in Figure 2.41, it can be noticed that the switching losses are greatly reduced, due to the clamping of the modulation wave for $60^o$ caused by the DPWM1 technique. Additionally, by looking at the total power losses, plotted in Figure 2.42 it can be seen that that they are highly dependent of the direction of the power flow within the system. During the acceleration and constant speed periods of the motor, the power will flow from the DC link towards the machine, thus stressing the transistor, while during the deceleration period, the power will flow from the PMSM towards the grid, thus more stress will be induced in the power diode.

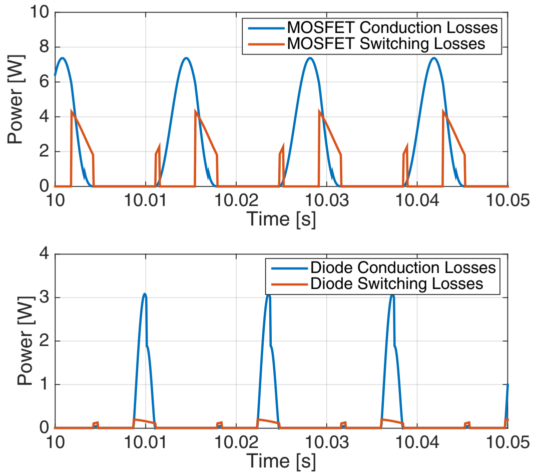


Figure 2.41: Conduction and switching losses

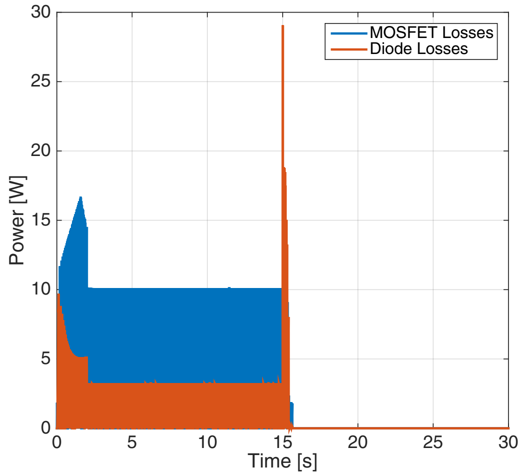


Figure 2.42: Total losses in power device

Finally, according to the input power losses of the devices and the estimated thermal parameters of the Foster network, the *Thermal Model* will compute the thermal cycles which appear in the power devices. As it can be seen in junction temperature plot of the transistor and diode, presented in Figure 2.43, some large temperature swings will occur during the start-up and deceleration periods of the motor, due to the large current amplitude and the low fundamental frequency operation of the converter.

It is clear that the thermal loading of the power diode will be more severe, due to its higher thermal impedance in comparison with the transistor. Furthermore, due to the high power losses generated by the diode when it is conducting current (deceleration period), these thermal cycles will be significantly amplified. Besides that, it can be noticed that the amplitude of the thermal cycles tends to increase as the machine decreases its speed and approaches the full stop state.

Therefore, based on the conclusions drawn in [6] and [7], the large thermal stress to which the power semiconductor devices are subject to during the start-up and braking periods of the motor, will lead to a faster degradation of the devices and will results in an unsatisfactory reliability performance of the motor drive.

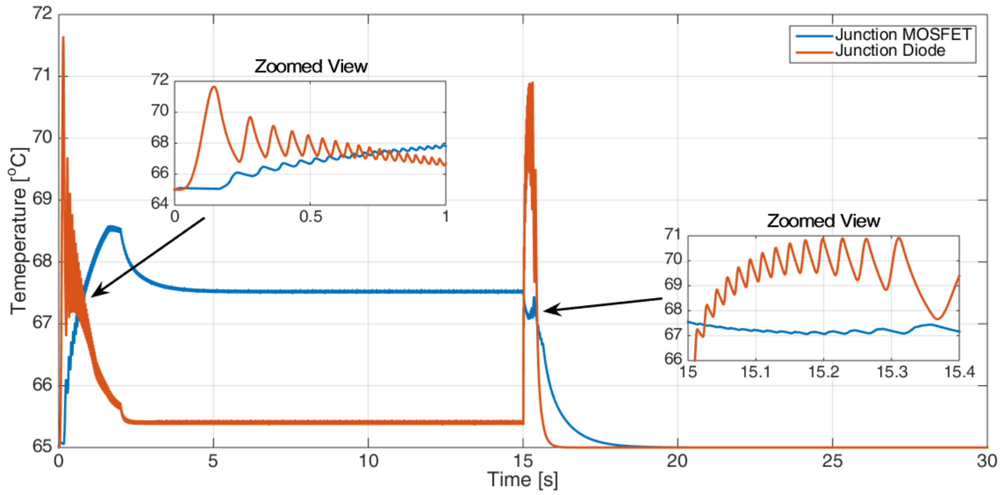


Figure 2.43: Junction temperature of the power device

# Chapter 3

# Active Thermal Control for Improved Lifetime of Power Devices

*This chapter commences by introducing the main parameters that cause adverse thermal stress in power devices and their impact on the junction temperature. Afterwards, a detailed description of the active thermal control methods will be presented, starting with the Switching Frequency Adjustment, followed by the Reactive Current Injection method. Finally, the active thermal control of power devices by adjusting the Deceleration Slope will be presented.*

As it was shown in the thermal cycling modelling chapter, the junction temperature of power semiconductor devices is highly dependent on the thermal impedance of the device and on the power losses to which it is subject to. Since the thermal impedance is solely dependent on the thermal properties of the materials of which the device is build and it is not adjustable, the influence of the power losses will be investigated.

In the analysis of the power loss model it has been concluded that the total power generated by a device consists of conduction losses and switching losses. One of the main parameters that influences both types of losses is the amplitude of the load current. Consequently, the current will have an important impact on the power device thermal cycling and its effect on the junction temperature of the MOSFET and power diode, has been presented in the previous section. Thus, the amplitude of the thermal cycles can be adjusted by controlling the output currents of the PMSM. A similar conclusion can be drawn regarding the other two controllable parameters involved in the loss modelling, the switching frequency and the DC link voltage, parameters which have a strong influence on the generated switching losses.

Furthermore, in [24], it has been shown that by injecting reactive power into the system, the thermal fluctuations of the power semiconductor devices can be adjusted, thus achieving a more uniform junction temperature during the load variation periods.

Therefore, in order to reduce the large temperature swings which appear the power devices, the following control methods will be implemented:

- *Switching Frequency Adjustment*
- *Reactive Current Injection*

Moreover, a novel thermal control method based on adjusting the deceleration slope of the PMSM is proposed:

- *Deceleration Slope Adjustment*

Finally, it should be noted that due to the limited amount of time available, only the deceleration period of the motor will be analyzed. Thus, the above mentioned control methods will be applied strictly during the period of time in which the motor is braking.

All the above mentioned control algorithms have been implemented to adjust the junction temperature of the power devices online, by means of Look-up Tables. Prior to that, offline simulation have been carried out in order to estimate the dependency of the of the junction temperature with respect to the following parameters: $f_{sw}$, $i_d$ and $\omega$. The results of the offline simulation have been linearized and and insert in a look-up table for on-line use. The general block diagram of the control methods is shown in Figure 3.1.

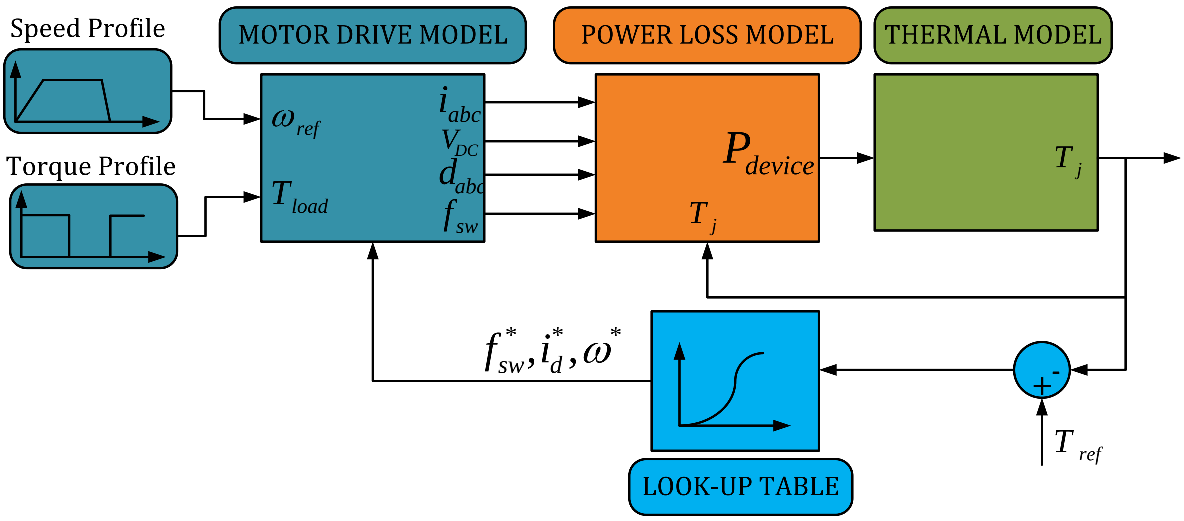


Figure 3.1: Look-up table based active thermal control

The same procedure has been utilized for all three methods, and therefore and block diagram is applicable for each one of them. Based on the thermal cycles estimation conducted, in the thermal model, the output junction temperature will be used as the feedback control loop. Therefore, the reference junction temperature will be comapred with the averaged junction temperature from the thermal model, and the error will be fed to the look-up table block. According to the offline estimation, the reference signal will be determined, and will fed as a control parameter to the motor drive model.

## 3.1 Switching Frequency Adjustment

This method has been intensively studied throughout the literature ([25], [26]) rendering satisfying results in terms of controlling the thermal loading of the power devices. The main idea behind this control method is to decrease the switching frequency of the converter, and therefore reducing the switching losses which occur in the power devices, respectively the thermal cycles. Although, it has some important disadvantages that need to be taken into consideration before applying this method. The main drawbacks are its complex implementation algorithm and the fact that by decreasing the switching frequency of the converter, output current ripple will be larger, and will lead to an increase in power losses in the motor [].

Since this is not the main purpose of this project, the machine losses will be neglected. Furthermore, due to synchronization reasons, the switching frequency will be decreased in multiple integer values of the switching frequency [25]. Therefore the following switching frequency steps have been taken into consideration: 4 [kHz], 8 [kHz] and 16 [kHz].

The system model together with the *Switching Frequency Adjustment* method have been implemented in Simulink, and the simulation has been run at nominal parameters. Since the inverter was modelled as a delay in the motor drive model, there is no actual visible effect of the decreased switching frequency of the motor drive waveforms.

On the other hand, by looking the the power device losses, shown in Figure 3.2, it can be seen that the switching losses of the MOSFET have significantly reduced during the deceleration period. Thus, from the junction temperature graph, plotted in Figure 3.3, a small decrease in the thermal loading of the MOSFET and on the power diode can be observed.

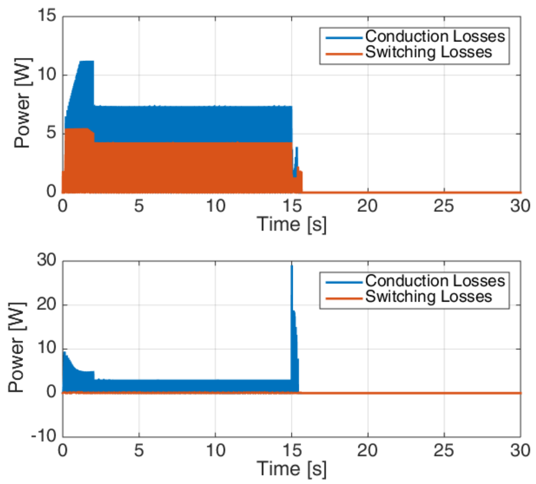


Figure 3.2: Power device losses

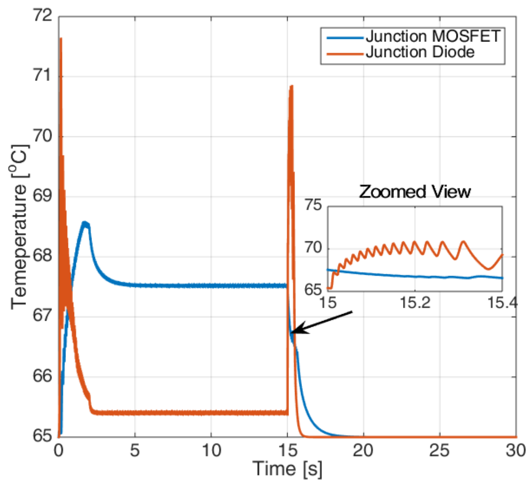


Figure 3.3: Power device junction temperature

The main reason behind the small impact that the this particular method has on the thermal loading is due to the low energy loss characteristics of the power devices used as study case. Furthermore, due to the fact that the DPWM1 technique is being employed, the switching losses are already reduced.

## 3.2 Reactive Current Injection

This method has been proposed in [24], where it has been shown that by injecting reactive power into the system, the thermal variations can be significantly reduced and power losses can be more equally distributed among the power semiconductor devices.

In Figure 3.4 the *dq* reference frame currents are shown, and the injection of negative reactive current into the system during the deceleration period can be observed. As expected, the amplitude of the phase currents, will increase during that period of time.

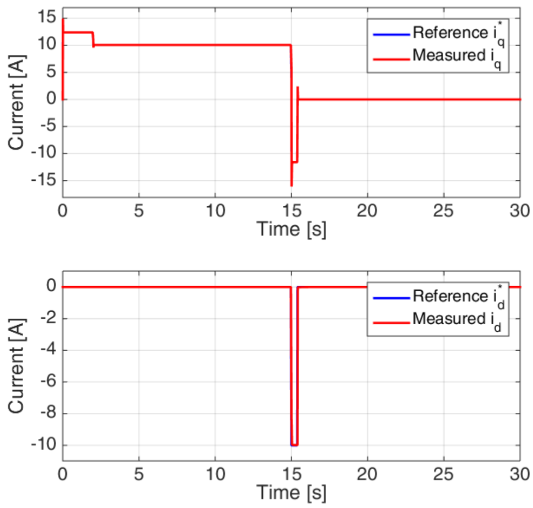


FIGURE 3.4: $i_d$ and $i_q$ currents

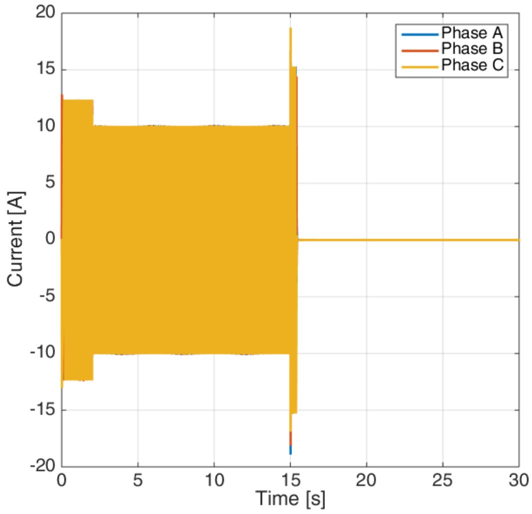


FIGURE 3.5: Phase currents

As it can be seen in Figure 3.6, the large amplitude current will have a strong impact on the diode power loss, and will put more stress on the diode. Although, this will lead to a higher thermal cycles induced in the power diode, in Figure 3.7 it can be noticed that the MOSFET temperature has increased with approximately $2^oC$, reaching the junction temperature value from the constant speed period. Therefore, the large drop in temperature which occurred during the braking period of the motor has been removed, resulting a smoother junction temperature waveform.

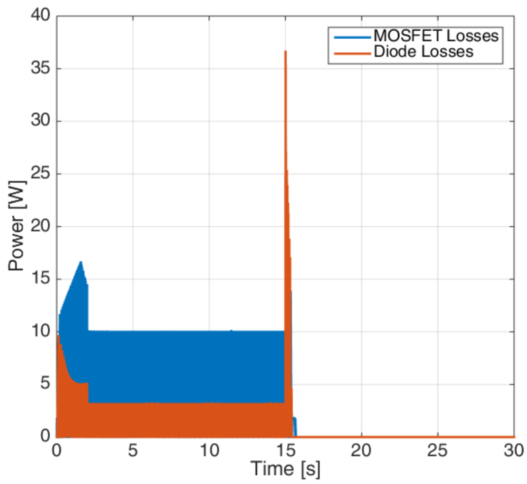


FIGURE 3.6: Total power losses of the device

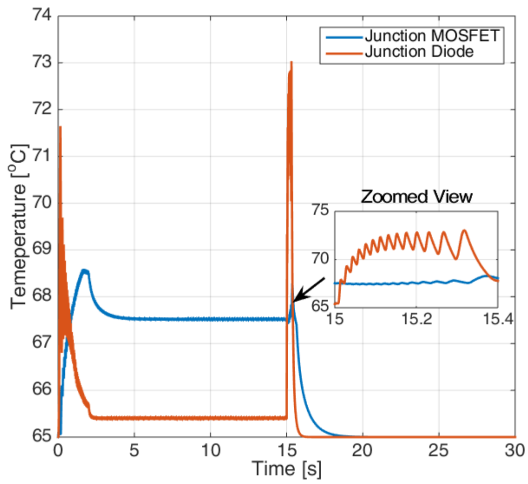


FIGURE 3.7: Power device junction temperature

## 3.3 Deceleration Slope Adjustment

Finally, the last proposed method consists of decreasing the amplitude of the current based on adjusting the deceleration slope of the speed profile. Similar, to the other two methods, the deceleration slope value will be determined by the Look-up Table block, according to the error resulting from the comparison between the average junction temperature and the reference junction temperature. Therefore, for a junction temperature reference equal to $66.5^oC$ the look-up table has computed a slope $m = -1.25$, resulting in a full stop of the motor after $1[s]$ after braking.

As it can be seen in Figure 3.8, an increase in the deceleration period of the motor by $0.6[s]$ will lead to a significant reduction of the electromagnetic torque overshoot and of the phase currents.

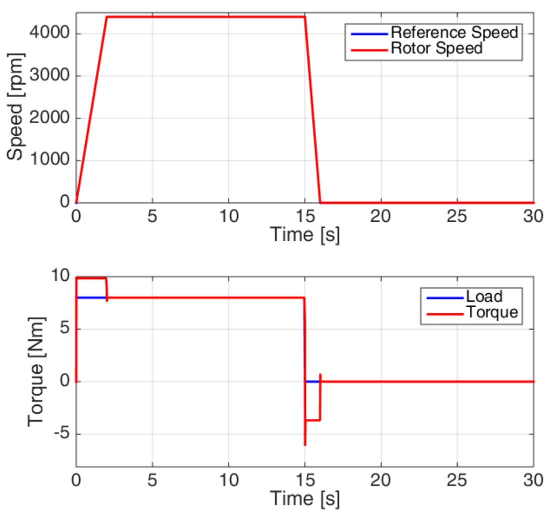


Figure 3.8: Speed & Torque response of the motor

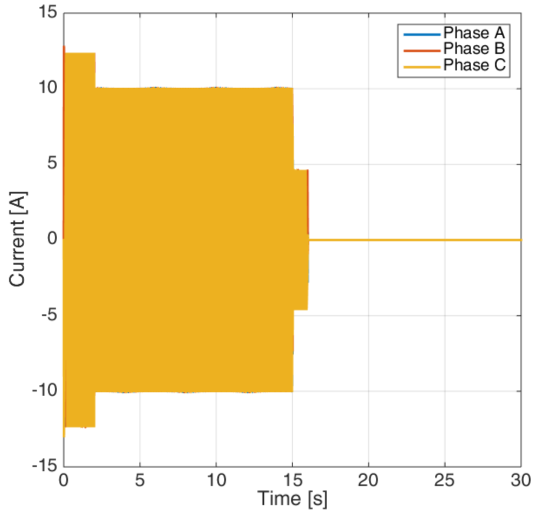


Figure 3.9: Phase currents

Due to the low amplitude currents, the conduction losses of the power devices are greatly reduced. Therefore, the large thermal cycles which occurred during the braking period of the motor are almost completely removed in the case of the MOSFET, while for the power diode, the amplitude of temperature swings has decreased dramatically.

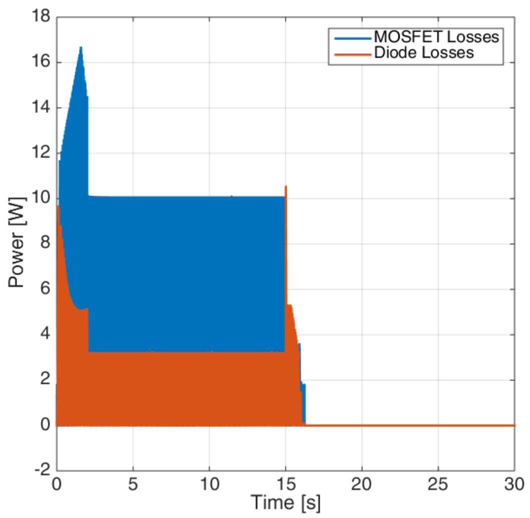


Figure 3.10: Total power losses of the device

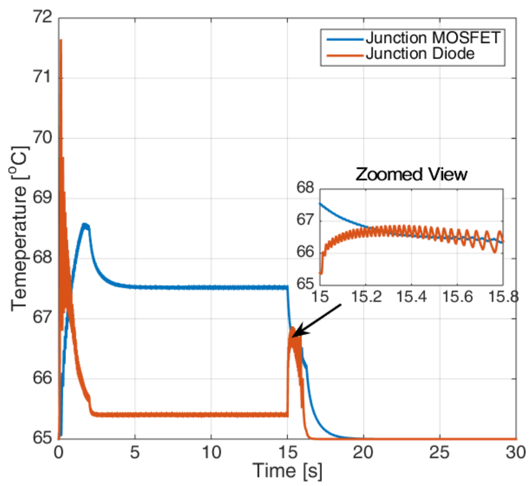


Figure 3.11: Power device junction temperature

Therefore, it can be concluded that decreasing the deceleration slope is the most effective method for the given application among the three active thermal algorithms presented.

# Chapter 4

# Experimental Validation

*Within this chapter, the experimental results will be shown. First, a detailed description of the laboratory setup is given, together with all its components and their role within the given laboratory setup. Afterwards, the motor drive mission profile emulation algorithm will be introduced, followed by a short description of Orthogonal Signal Generator and the current controller used in order to generate the reference signals for the PWM modulation technique. Finally, the simulation results obtained from the mission profile emulation algorithm will be validated by means of experimental work.*

## 4.1 Laboratory Setup

In order to validate the simulation results presented in the previous chapter, the experimental setup shown in Figure 4.1 has been used. In order to eliminate the need for an actual motor drive system, and to facilitate the thermal measurement of the junction temperatures of the power devices, a three level NPC H-bridge is employed. The setup allows the emulation of different mission profiles of various real-life applications, among which, motor drive systems. Therefore, the motor drive load conditions will be emulated on the inductive load of the setup and on power semiconductor devices. For further understanding, a detailed block diagram of the setup is shown in Figure 4.2.

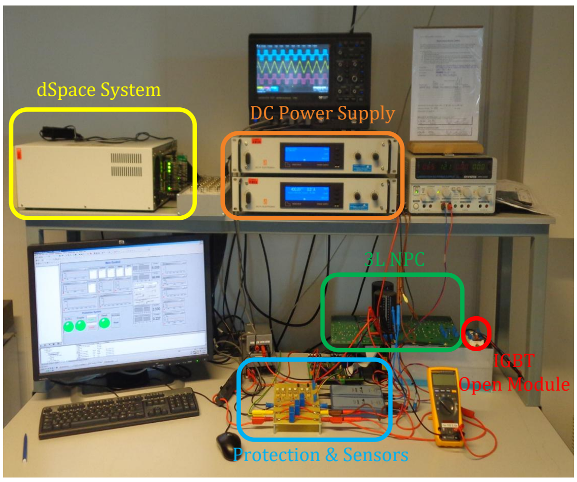


Figure 4.1: Experimental setup

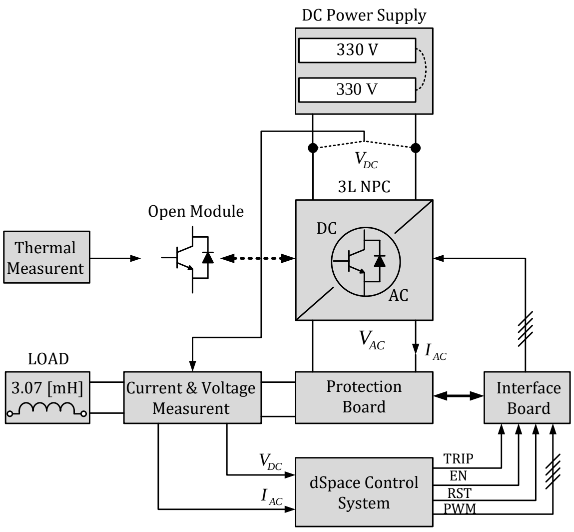


Figure 4.2: Experimental setup block diagram

The input DC voltage of the system will be provided by two *Delta Electronik* DC power supplies, each capable of generating maximum 330V at the output. In order to achieve a more precise voltage balancing on the capacitors of the NPC, the DC sources are connected in series through a Master/Slave Unit. Thus, the Master Unit will supply a full DC voltage of maximum 660V, which will be equally distributed among the two capacitors.

The inverter used in this application is a 10 [kW] neutral point clamped H-bridge, which has the main puspose of providing an AC voltage to the load. The converter is shown in Figure 4.3, and from its electrical circuit diagram shown in Figure 4.4, it can be noted that the inverter is formed of two legs: the load leg and the test leg. The test leg is responsible for generating and controlling the AC voltage according to the imposed modulation index and fundamental frequency requirements, while the load leg is used in order to control the output current [27].

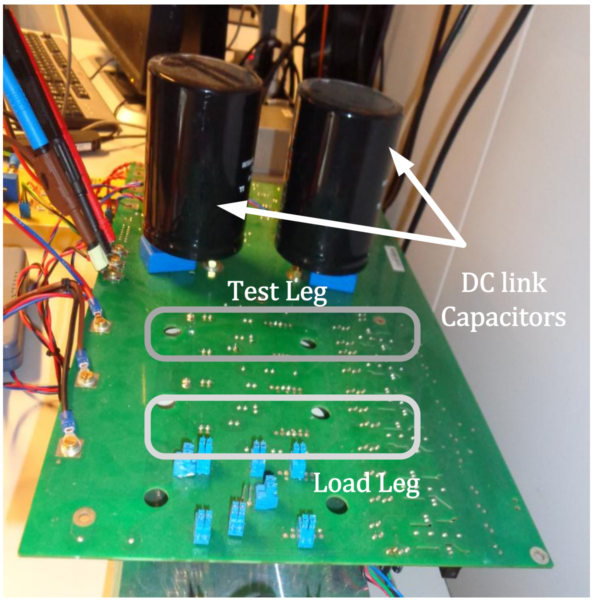


Figure 4.3: H-bridge NPC inverter

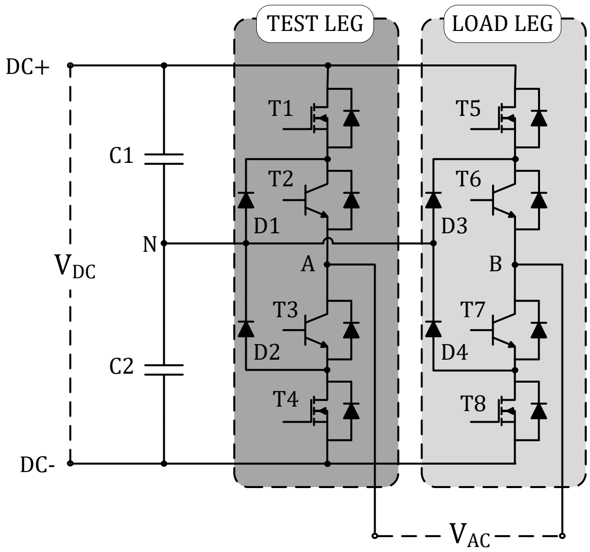


Figure 4.4: Circuit diagram of H-bridge NPC

Due to the physical limitations of the system, the protection board shown in Figure 4.5 will be employed, thus assuring over-voltage and over-current protection of the system. If the voltage or current values exceed the imposed limitations ($V_{DC_{max}} = 700[V]$ and $I_{\text{max/min}} = \pm 25[A]$), the protection will be tripped and no voltage/current will be supplied to the load.

If the values are within limits, voltage and current sensors are used to measure the DC link voltage and the load current, which will then be fed to the dSpace Control System measuring board, hence representing the feedback from the physical system. Based on the feedback response of the system, the voltage and current control will take place in the dSpace System according to the set mission profile inputs. The output of the dSpace System will represent the PWM signals for the inverter, which will be fed into the NPC interface board, presented in Figure 4.6. Finally, the interface board will transmit the switching sequence of the active semiconductor devices towards the load leg and the test leg of the inverter, thus closing the system control loop.

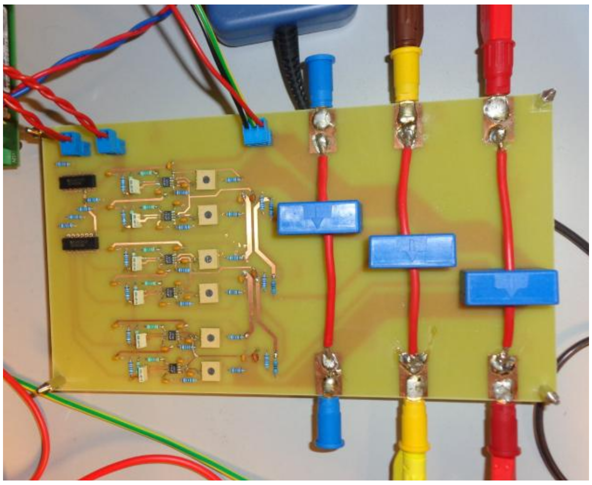

Figure 4.5: Protection board

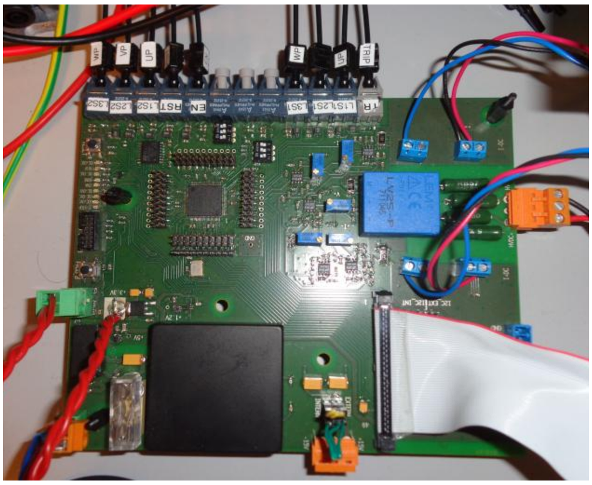

Figure 4.6: NPC interface board

Due to the fact that the active semiconductor devices of the inverter are encapsulated, thus making it extremely difficult to have a precise estimation or measurement of its thermal stress, an open IGBT module is used. The open module and its chips are shown in Figure 4.7. The open module is connected to the inverter through a bridge circuit, as shown in Figure 4.8, which will bypass the test leg of the inverter and will forward the gate signals towards the open module. It should be noted that the protection board, NPC interface board and the circuit bridge were not developed during this project.

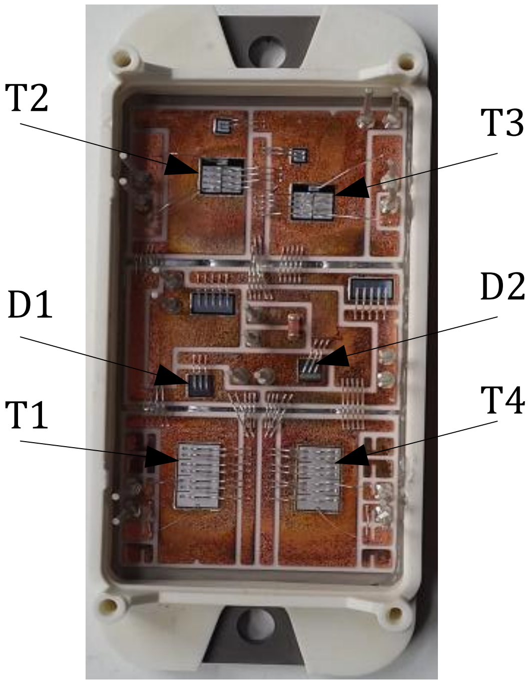


Figure 4.7: IGBT open module

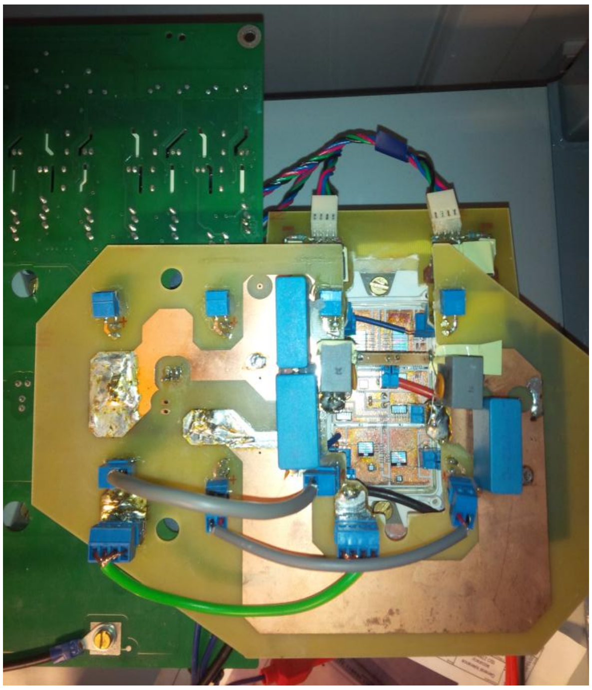

Figure 4.8: IGBT open module bridge

## 4.2 Mission Profile Emulation

In order to apply a similar stress on the power devices, as in the simulation model, the motor drive mission profiles need to be emulated on the experimental inductive load. This can be easily achieved by manipulating the *dq* reference frame equations of the PMSM, presented in Chapter 2.

As it can be seen in Figure 4.9, the *Mission Profile Emulation* block will provide all the necessary reference inputs for the current and voltage control algorithm, while the measured AC current supplied by the test leg, will first go through a Orthogonal Signal Generator (OSG) block, in order to generate the $\alpha\beta$ reference frame components of the current. The modulation index resulted from the dividing the the reference test voltage to the measured DC link voltage will be fed directly to the PWM generation block, thus determining the switching sequence of the test leg active devices. On the other hand, the PWM signals for the load leg are obtained according to the modulation index corresponding to the reference load voltage, which can be determined by means of current control.

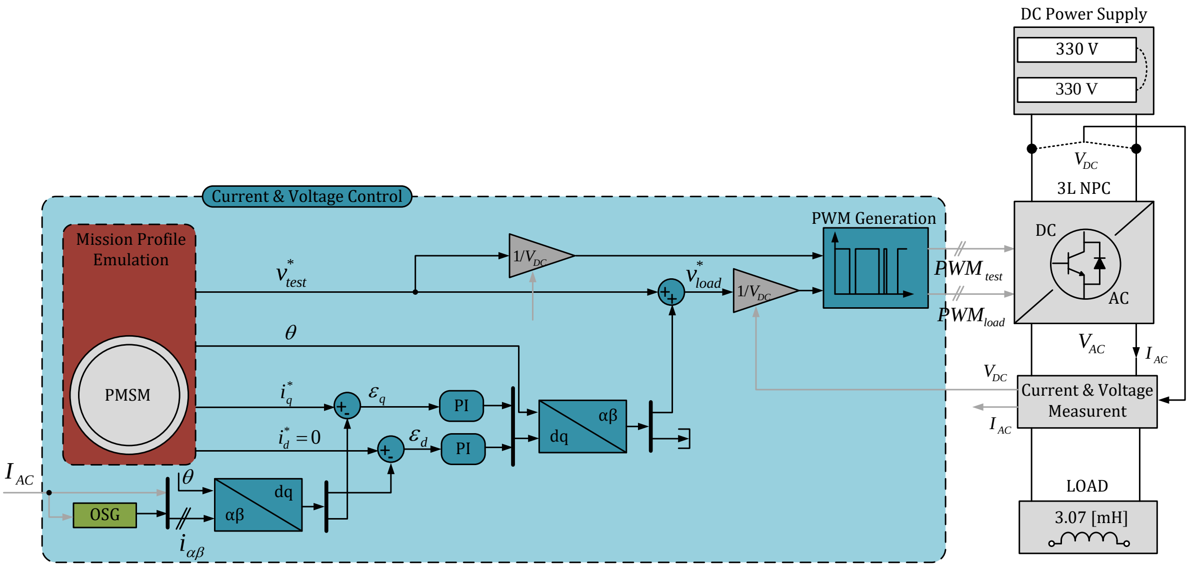


FIGURE 4.9: dSpace - Simulink model

### 4.2.1 Motor Drive Mission Profile

Based on the torque and speed profiles, the mechanical equation of the machine (Equation 2.7) can be rearranged so that the angle $\theta$ and the electromagnetic torque $T_e$ can be obtained, as shown in the following:

$$\theta = \int \omega_{ref} \cdot \frac{2\pi}{60} \tag{4.1}$$

$$T_e = \left( \frac{d\left(\frac{\omega_{ref} \cdot 2\pi}{60}\right)}{dt} \cdot J \right) + T_{load} \tag{4.2}$$

where, $\omega_{ref}$ represents the input speed mission profile, and $T_{load}$ represents the torque mission profile.

Therefore, by substituting the torque and electrical speed values into the torque equation (Equation 2.6) and the voltage equations (Equation 2.2 and Equation 2.3), the q-axis reference current and reference voltage of the test leg can be determined in quite straightforward manner. Similarly to the simulation model, the d-axis current reference $i_d^*$ is set to 0.

$$i_q^* = \frac{2 \cdot T_e}{3 \cdot \psi_{pm} \cdot n_{pp}} \tag{4.3}$$

$$v_d^* = R_s i_d^* + L_d \frac{di_d^*}{dt} - \omega \psi_q \tag{4.4}$$

$$v_q^* = R_s i_q^* + L_q \frac{di_q^*}{dt} + \omega \psi_d \tag{4.5}$$

Finally, the $\alpha$ voltage component obtained by applying the inverse Clarke transformation to the reference d- and q-axis voltages will represent the reference voltage for the test leg. The detailed block diagram of the *Mission Profile Emulation* is shown in Figure 4.10.

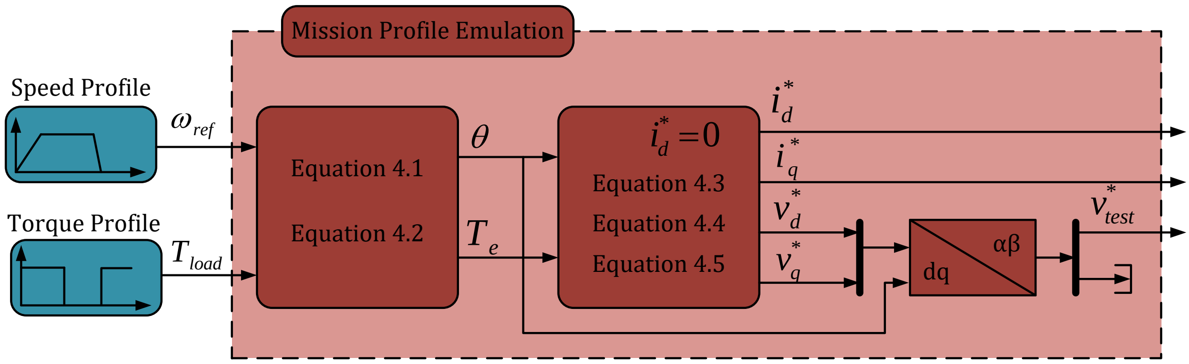


Figure 4.10: Mission Profile Emulation block diagram

### 4.2.2 Orthogonal Signal Generator

It order to be able to control the AC current generated by the NPC H-bridge, its *dq* reference frame components need to be compared with the reference currents $i_{dq}^*$. Thus, the current must go through the Clarke and Park transformations. In order to obtain the $\beta$ component of the current a Orthogonal Signal Generator is used. Many techniques of generating the orthogonal signal component have been studied throughout the literature, but due to the nature of the given application, the variable transport delay and Second Order Generalized Integrator (SOGI) methods have been concluded to be the most suitable approaches.

The Variable Transport Delay method has the main advantage of having an easy implementation, using only a First-in-First-Out (FIFO) buffer, as it can be seen in Figure 4.11. The size of the buffer will be changed according to the input frequency delay, generated by the motor drive mission profile. The disadvantages of using this method consist of relatively high error during the low frequency operation and the fact that it does not filter the output $\beta$ component [28].

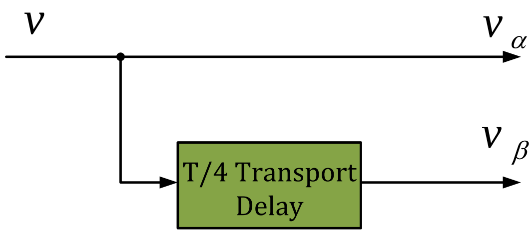


Figure 4.11: Transport Delay

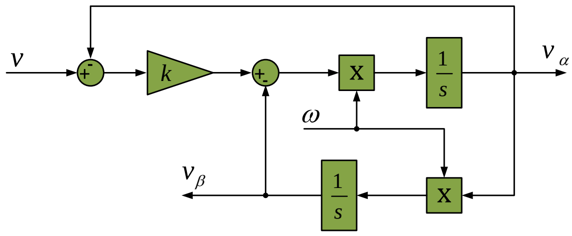


Figure 4.12: Second Order Generalized Integrator

The SOGI based method, presented in Figure 4.12, has been proved to render better overall dynamic performance in terms of generating the orthogonal component of an input signal. According to the input signal $v$ and frequency $\omega$ of the motor in [rad/s], the SOGI method will generate two sinusoidal waveform delayed by $90^o$, where $v_\alpha$ will present the same magnitude and frequency as the input signal. For the given study case, the value of the internal gain of the method $k$ has been chosen as twice the value of the damping ratio $\zeta$, thus $k = 2{\cdot}\zeta = 1.414$ [28].

Both methods, have been tested for a 4 [A] current mission profile, and as it can be seen in Figure 4.13 and Figure 4.14, both methods are able to accurately generate the $\beta$ component of the input AC current signal during constant speed operation. The limitations of the variable transport delay method can be seen during the low frequency operation and during the amplitude phase change state of the current. During these periods of time the method is displaying relatively high errors. On the other hand, the SOGI method seems to follow accurately the input current signal even at low frequency, while the error generated by the amplitude change of current is significantly lower that for the variable transport delay method.

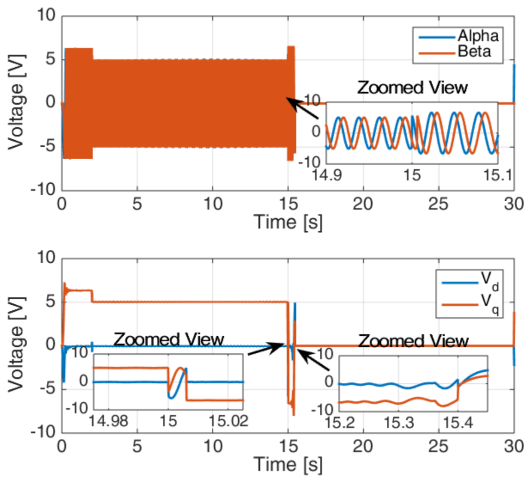


Figure 4.13: Variable transport delay

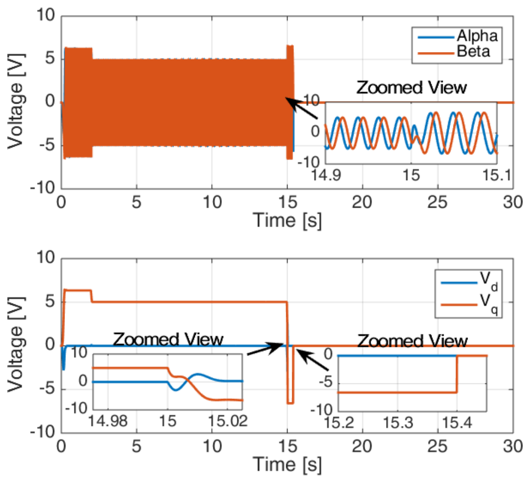


Figure 4.14: SOGI

### 4.2.3 Current Controller

The design of the current controller used in the mission profile emulation algorithm is similar to the one presented in Chapter 2, and will have the same main requirement: the overshoot should not exceed 5%. Therefore, only a brief description will be shown. The current control loop, shown in Figure 4.15, takes into account the delays added by the PWM generation and by the current measurement, which are modelled as first order systems, with a sample time of $T_s = 1/f_{sw} = 0.0625[ms]$. According to the load used in experimental setup, the plant transfer function can be derived as follows:

$$G(s) = \frac{1}{L \cdot s + R} \tag{4.6}$$

where, L represents the inductance and R is the internal resistance of inductor. Since the value of the internal resistance was not specified on the nameplate of the inductor, it is assumed equal to $0.001[\Omega]$.

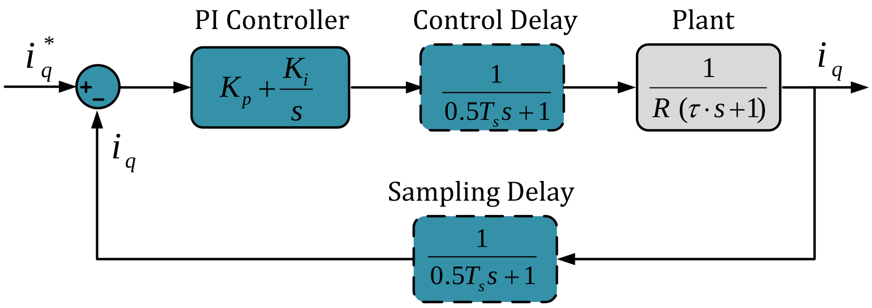


FIGURE 4.15: Current control loop

Similarly, to the motor drive current PI design, the Optimal Modulus criterion is applied, resulting in the following values of the proportional and integral gains:

$$K_p = 12.27$$
$$K_i = 101.3$$

Based on the determined controller parameters, the Bode diagram of the open loop system is plotted in Figure 4.16, and it can be seen the system is stable. Moreover, from the step response of the closet loop system, presented in Figure 4.17, it can be concluded that the controller meets the imposed requirement, due to the fact that the overshoot is equal to 4.75%.

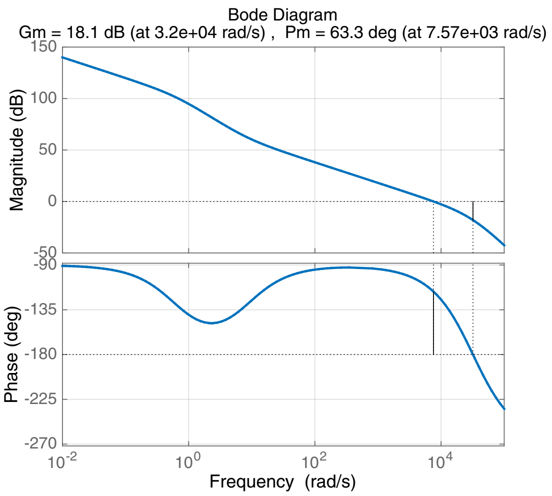


FIGURE 4.16: Current Control - Bode Diagram

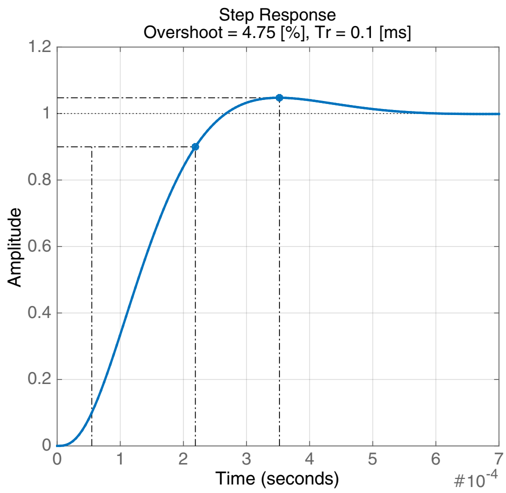


FIGURE 4.17: Current Control - Step Response

## 4.3 Simulation and Experimental Results

The above mentioned model has been implemented in MATALB/Simulink and linked with the dSpace system, with a sample time of $T_s = 1/16000[s]$. The experiment was run at 660V DC input, and the output AC voltage of the inverter can be seen Figure 4.19. It can be observed that the test and load leg voltages are in phase and that the waveforms are generated in three voltage steps ($V_{dc}/2$, 0 and $-V_{dc}/2$) due to the three level configuration of the NPC.

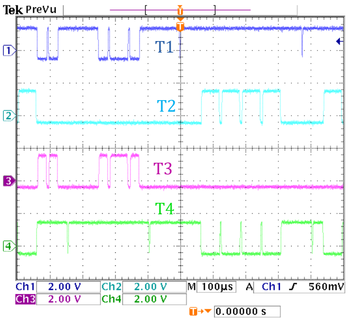


Figure 4.18: Test leg PWM

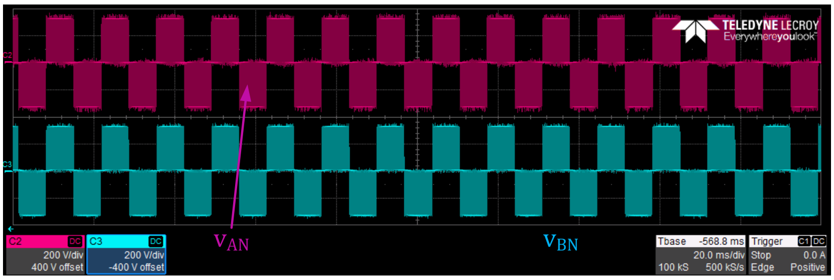


Figure 4.19: Inverter output voltage

In Figure 4.20 the simulation results obtained after emulating the motor drive speed and torque mission profiles, on the three level NPC H-bridge can be seen. It can be noticed that emulation is performed in a correct manner, the obtained waveforms, resembling the current and voltage response of the PMSM. In order to highlight the correlation between the voltage and current, the plotted voltage waveform has been divided by a factor of 10.

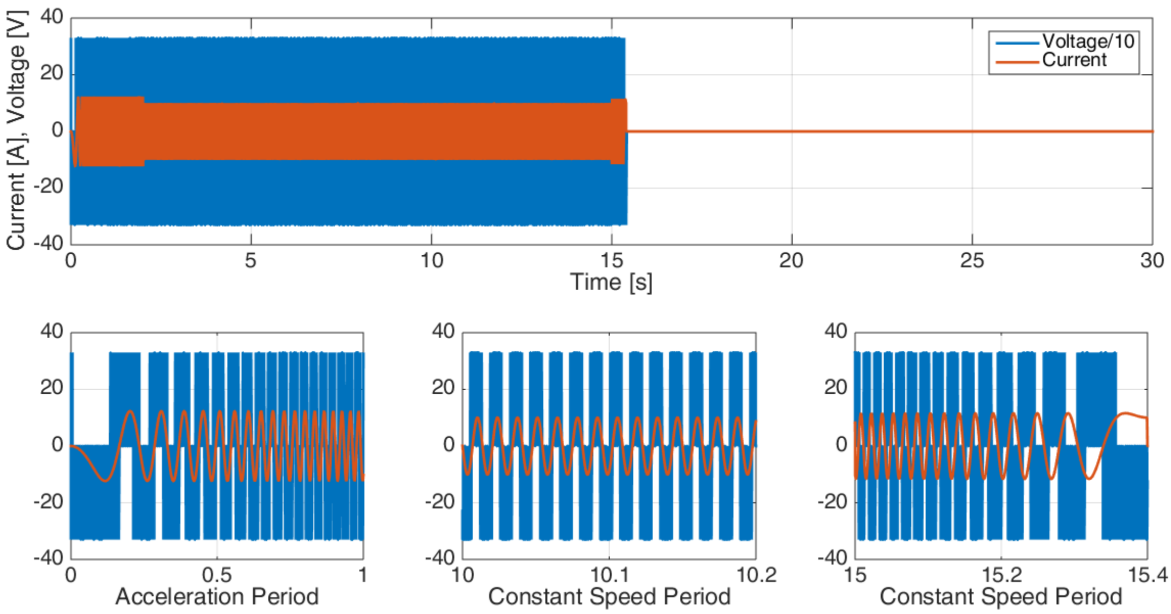


Figure 4.20: Normal operation - Mission profile

The results obtained from running the experiment at Normal Operation mission profile can be seen in Figure 4.21. From the full view of a single cycle of the mission profile, shown in Figure 4.21a, it can be observed that the current waveform matches the simulation results, with some minor errors on the deceleration period.

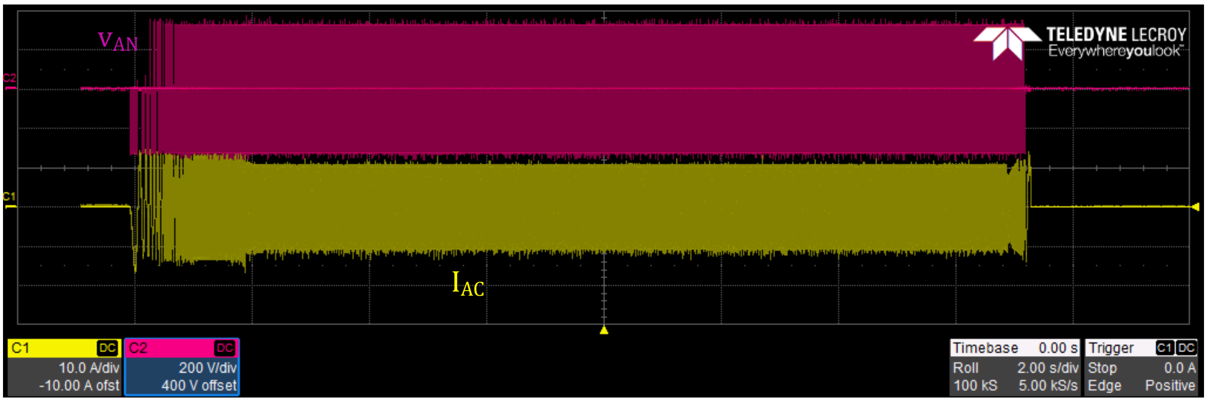


(A) Mission Profile - Full view

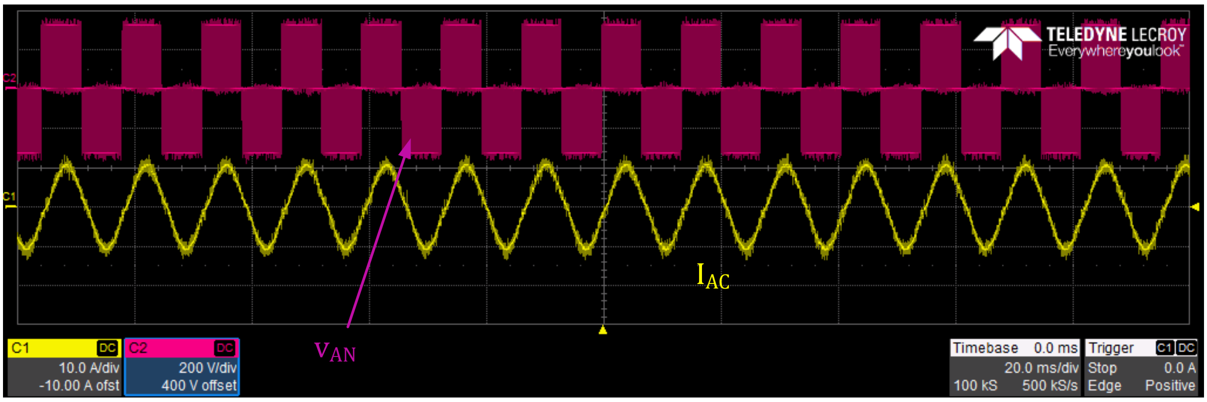


(B) Zoomed View - Constant speed

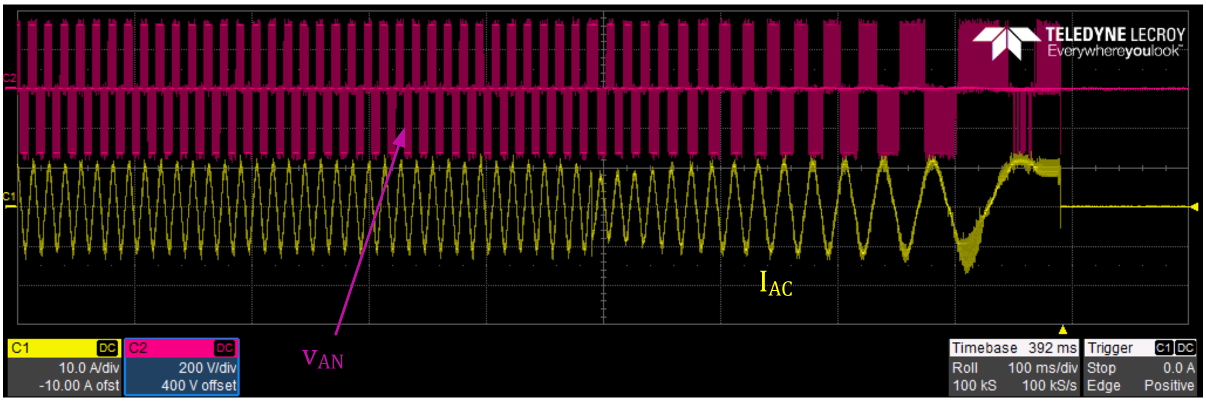


(C) Zoomed View - Deceleration

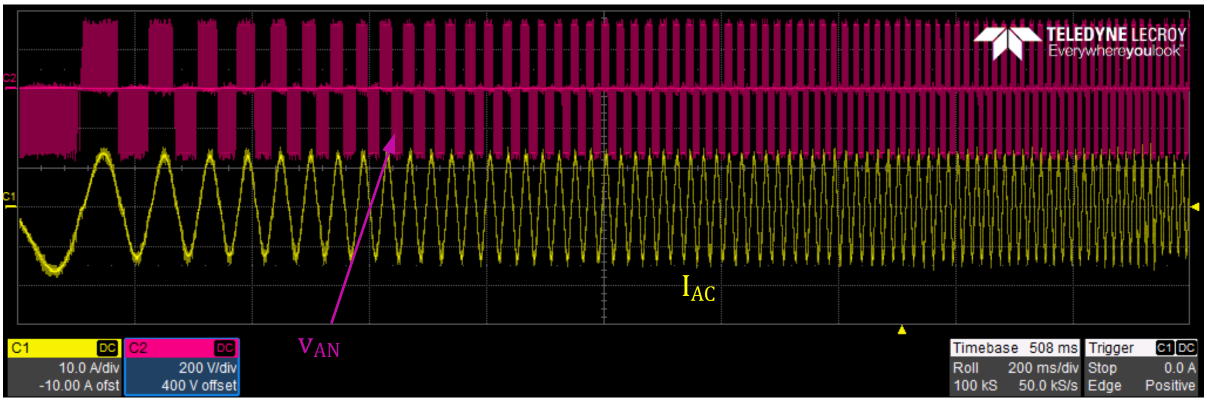


(D) Zoomed View - Acceleration

Figure 4.21: Normal operation mission profile

During the constant speed operation the current reaches the reference 10 [A] value and runs in phase with the test leg voltage at a frequency of approximately 73 [Hz]. Although, during the acceleration period the system behaves as expected, with the current hitting its estimated 12 [A] value, during the deceleration period the current presents a long response time reaching its reference value in roughly 0.2 [s]. This is mainly due to the error rendered by the OSG block when the current goes through a large amplitude change (from 10 [A] to -12 [A]). Moreover, as the frequency of the drive is decreasing the error caused by the variable time delay increases, which will result in high noise in the current waveform, as shown in Figure 4.21c.

In order to solve this problem, the Second Order Generalized Integrator (SOGI) was used to generate the quadrature of the output current, but the discrete-time domain implementation of this method rendered a similar error during the low frequency operation. Therefore, due to time limitations, this issue was no longer investigated and the variable transport delay based OSG has been employed for the other cases.

*A. Deceleration Slope Adjustment*

In the following the decreased deceleration slope mission profile is presented. In Figure 4.22 the simulation results are presented.

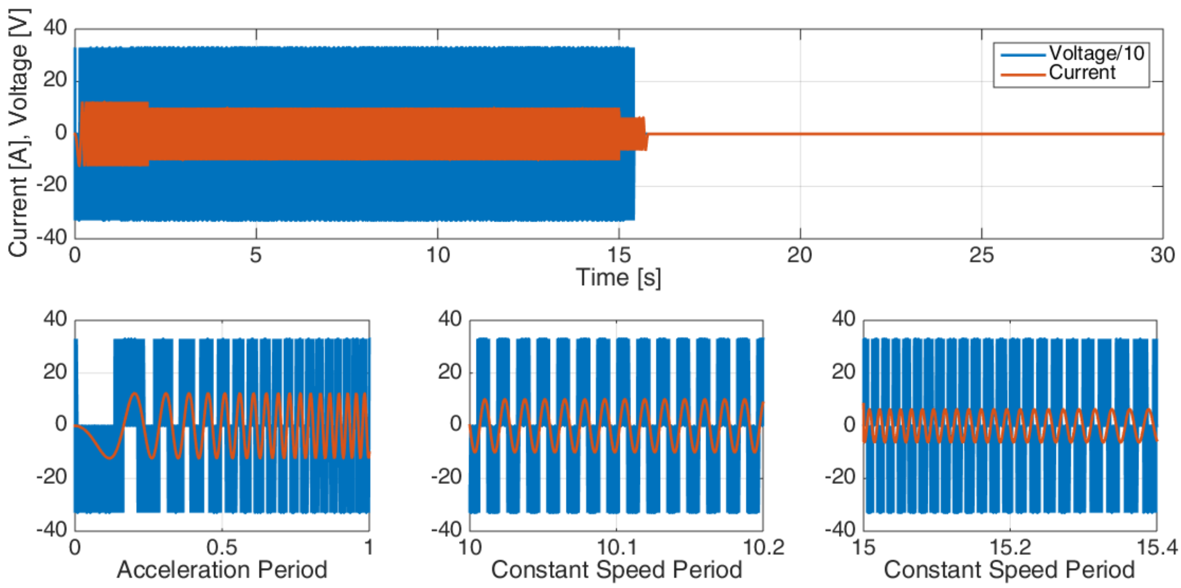


Figure 4.22: Deceleration Slope Adjustment - Mission profile

In Figure 4.23, the results obtained from emulating the Decreased Deceleration Slope profile can be seen. As expected, during the deceleration period, the amplitude of the current is significantly reduced, but similarly to the previous case, a long response time can be observed. The behaviour of the current in the acceleration and constant speed time periods is identical to the Normal Operation mission profile.

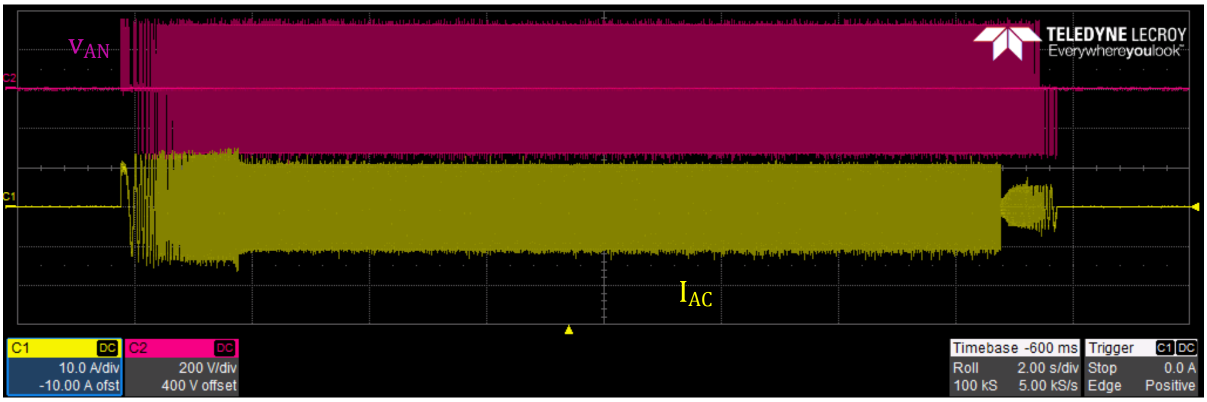


(A) Mission Profile - Full view

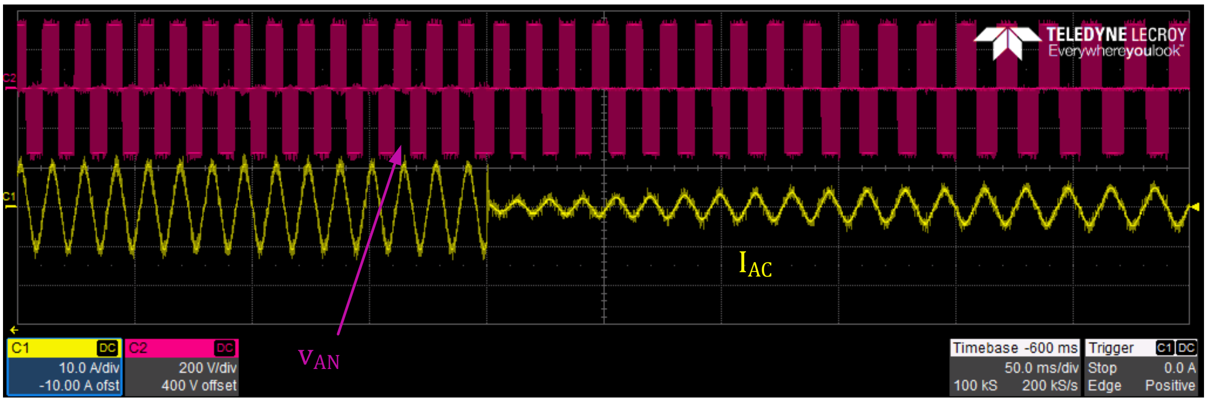


(B) Zoomed View - Deceleration

Figure 4.23: Decreased deceleration slope mission profile

*B. Reactive Current Injection*

In the following, the system response will be analyzed during the reactive current injection case, as shown in Figure 4.25, while the simualtion results are shown in Figure 4.24.

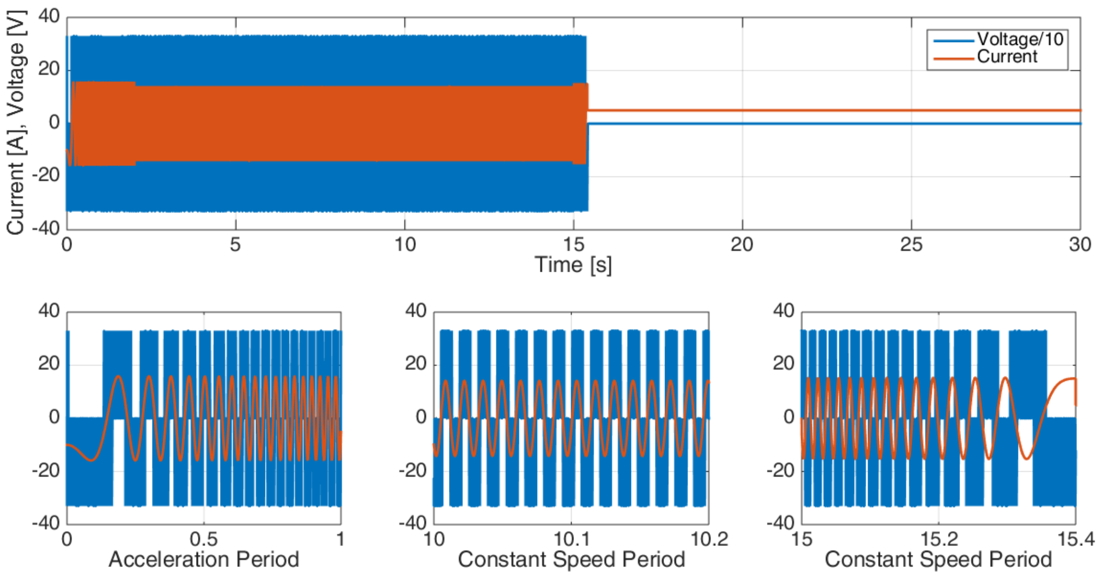


Figure 4.24: Reactive Current Injection - Mission profile

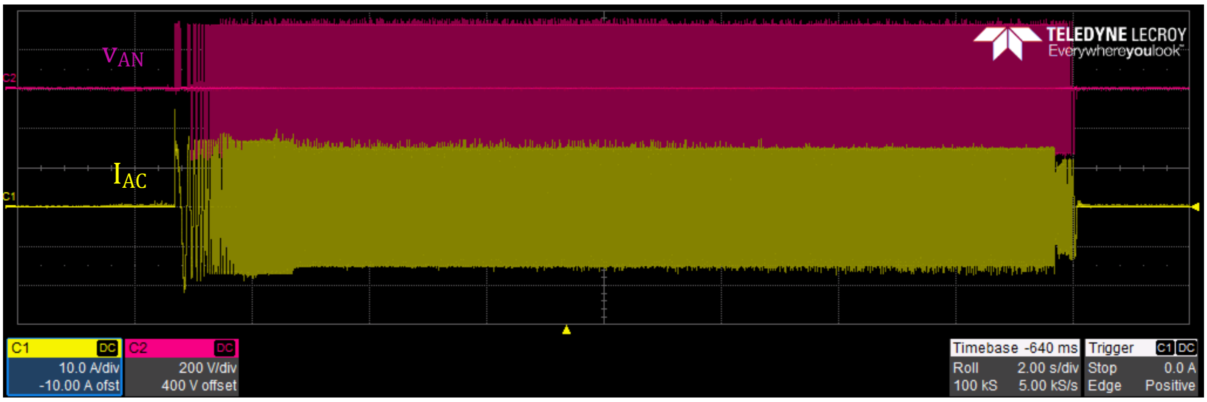


(A) Mission Profile - Full view

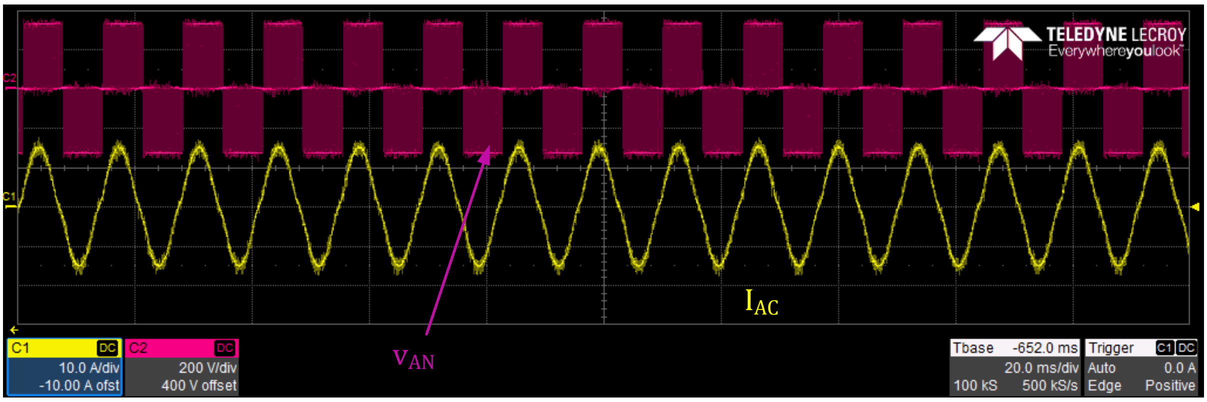


(B) Zoomed View - Constant speed

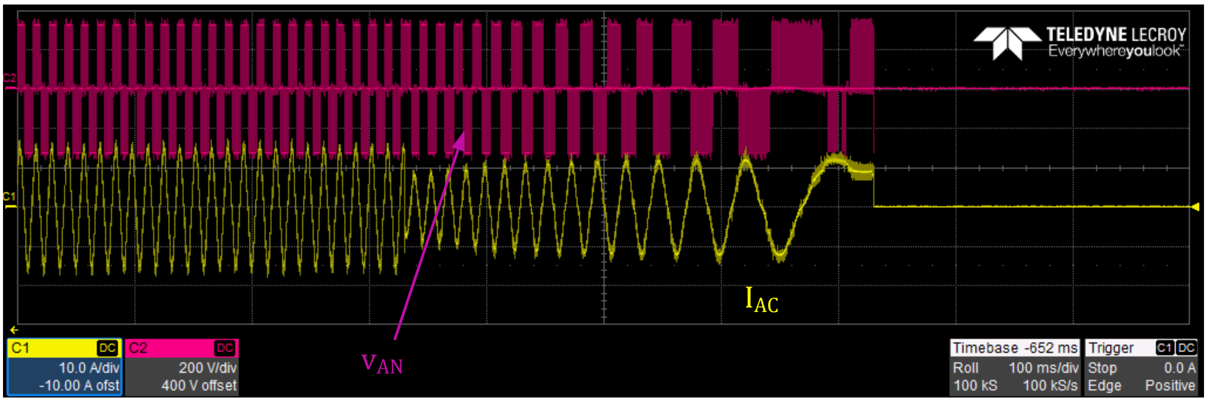


(C) Zoomed View - Deceleration

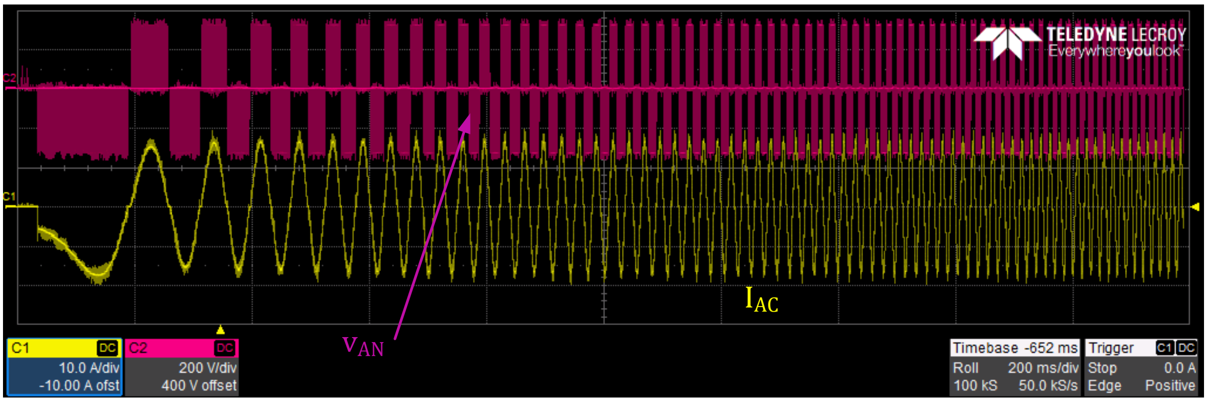


(D) Zoomed View - Acceleration

Figure 4.25: Reactive current injection mission profile

By injecting reactive current ($i_d^* = -10[A]$) into the system, the expected current amplitude will increase in comparison with the previous two cases. In Figure 4.25b - Figure 4.25d, it can also be observed that the current waveform is leading the voltage. On the other hand, if the injected reactive current is positive ($i_d^* = 10[A]$) the current will be lagging the voltage, as presented in Figure 4.27, while the simulation results for pozitive reactive current injection are shown in Figure 4.26

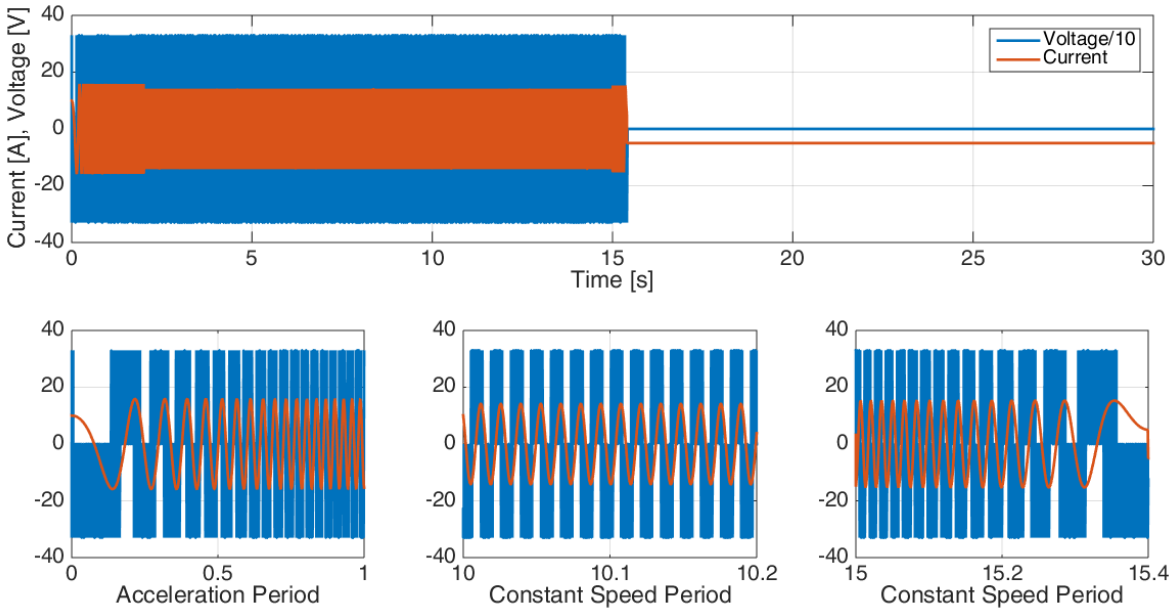


Figure 4.26: Reactive Current Injection - Mission profile

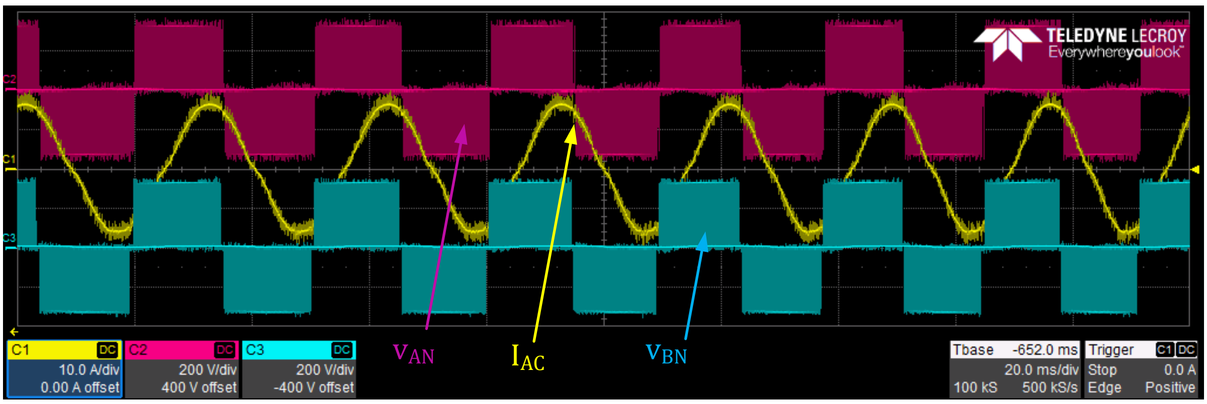


Figure 4.27: Zoomed View - Constant speed

### *C. Switching Frequency Adjustment*

At this point it should be noted that the Decreased Switching Frequency case was not analyzed, due to the limitations of the dSpace system, which can not change the fixed-step sample size during a real-time simulation.

# Chapter 5

# Conclusions

In this thesis, three active thermal control methods for the power semiconductor devices of the motor drive application have been investigated.The motor drive system together with the thermal loading which occurs in the power semiconductor devices has been modelled and the dynamic behaviour of the system has been analyzed under certain speed and torque mission profiles. During the acceleration and the deceleration periods of the motor, large thermal cycles, could be observed in the power devices. It has been concluded that the main causes for this large temperature swings are the amplitude of the load current of the machine and the low fundamental frequency. Additionally, the influence of the parameters involved in the power loss modelling has been investigated and it has been concluded that the switching frequency and the DC link voltage will have a significant impact on the thermal stress to which the power devices are subject to.

In order to solve the aforementioned problem, three active thermal control have been implemented. The *Switching Frequency Adjustment* method consists of decreasing the switching frequency of the converter, and therefore reducing the switching losses of the devices. The method has proved effective in decreasing the amplitude of the amplitude of the thermal cycles, but due to the low switching loss characteristics of the power devices used as study case, the impact of the method is not significant.

Afterwards, the *Reactive Current Injection* method has been analyzed, managing to eliminate the large temperature drop from the braking period of the motor, thus leading to a more uniform thermal distribution. Finally, the *Deceleration Slope Adjustment* method has been investigated, and it has been concluded that it is the most effective algorithm among the other presented, for the given application.

In order to validate the simulation results, a motor drive mission profile algorithm has been developed. The speed and torque mission profiles have been translated to the reference voltage and current values needed within the experimental setup control algorithm. The AC current controller used in the mission profile emulation has been design, and an orthogonal signal generator has been implemented. By employing the algorithm, the speed and torque mission profile were successfully emulated on the inductive load of the experimental setup, thus validating the emulation technique simulation results.

## 5.1 Future work

One of the first steps that should be followed as future work, is to measure the thermal loading on the open IGBT module. A layer of black paint has been applied to the power module, as shown in Figure 5.1, in order to facilitate an accurate temperature measurement of the junction temperatures of the power semiconductor devices.

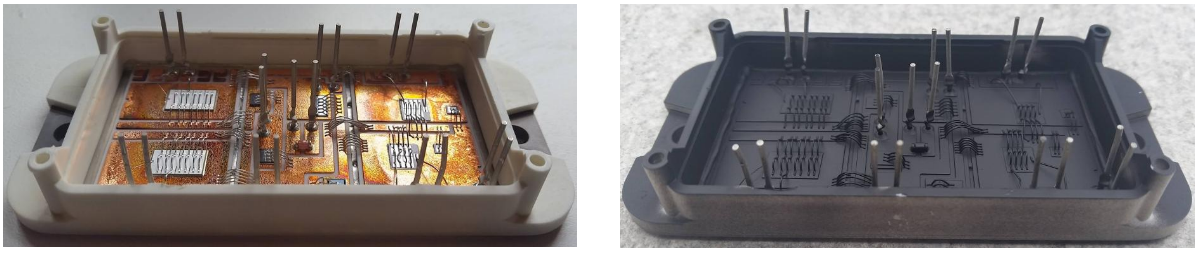

(a) Before (b) After

Figure 5.1: IGBT open module

Once the actual thermal measurement validate the obtained thermal results, the active thermal control algorithms can be implemented in the experimental setup, in order to confirm the effectiveness of the methods.

Additionally, the problem of the orthogonal signal generation should be further investigated, especially for the low fundamental frequency operation.

# Bibliography


[1] N. Mohan, T.M. Undeland, and W.P. Robbins. *Power Electronics: Converters, Applications and Design.* John Wiley and Sons Inc., 2014.

[2] L.M. Moore and H.N. Post. *Five Years of Operating Experience at a Large, Utility-scale Photovoltaic Generating Plant.* Prog. Photovolt: Res. Appl., 2008.

[3] Juan Bueno Gayo. *Reliability-focused research on optimizing Wind Energy system design, operation and maintenance: Tools, proof of concepts, guidelines & methodologies for a new generation.* 2011.

[4] S. Yang, A. Bryant, P. Mawby, D. Xiang, L. Ran, and P. Tavner. *An Industry-Based Survey of Reliability in Power Electronic Converters.* 2009.

[5] ZVEI: Die Elektroindustrie. *Handbook for Robustness Validation of Automotive Electrical/Electronic Modules.* German Electrical and Electronic Manufacturers Association, June 2013.

[6] U.Choi. *Studies on IGBT Module to Improve the Reliability of Power Electronic Systems.* Aalborg University Press, Feb.2016.

[7] V. Smet, F. Forest, J.-J. Huselstein, F. Richardeau, Z. Khatir, S. Lefebvre, and M. Berkani. *Ageing and Failure Modes of IGBT Modules in High-Temperature Power Cycling.* IEEE Trans. on Industrial Electronics, Vol. 58, No. 10, Oct.2011.

[8] A. Wintrich, U. Nicolai, W. Tursky, and T. Reimann. *Semikron: Application Manual Power Semiconductors.* SEMIKRON International GmbH, 2015.

[9] M.S. Merzoug and F. Naceri. *Comparison of Field-Oriented Control and Direct Torque Control for Permanent Magnet Synchronous Motor (PMSM).* World Academy of Science, Engineering and Technology, 2008.

[10] X.T. Garcia, B. Zigmund, A. Terlizzi, R. Pavlanin, and L. Salvatore. *Comparison between FOC and DTC strategies for Permanent Magnet Synchronous Motor.* Advances in Electrical and Electronic Engineering, 2006.

[11] G.F. Franklin, J.D. Powell, and A.Naeini. *Feedback control of dynamic systems.* Boston : Pearson, 2006.

[12] C. Capitan. *Torque Control in Field Weakening Mode.* Aalborg University Press, 2009.

[13] M. Valentini, T. Ofeigsson, and A. Raducu. *Control of a variable speed variable pitch wind turbine with full power converter.* Aalborg University Press, 2007.

[14] R. Mizera. *Modification of Symmetric Optimum Method.* ASR 2005 Seminar, Instruments and Control, 2005.

[15] A.M. Hava, R.J. Kerkman, and T.A. Lipo. *Simple Analytical and Graphical Methods for Carrier-Based PWM-VSI Drives.* IEEE Trans. on Power Electronics, Vol. 14, no. 1, Jan.1999.

[16] M. Weckert and J. Roth-Stielow. *Lifetime as a Control Variable in Power Electronic Systems.* Emobility - Electrical Power Train, Nov.2010.

[17] G. Lo Calzo, A. Lidozzi, L. Solero, F. Crescimbini, and V. Cardi. *Thermal Regulation as Control Reference in Electric Drives.* Power Electronics and Motion Control Conference (EPE/PEMC), Sept.2012.

[18] A.T. Bryant, P.R. Palmer P.A. Mawby and, E. Santi, and J.L. Hudgins. *Exploration of Power Device Reliability Using Compact Device Models and Fast Electrothermal Simulation.* IEEE Trans. on Industry App., Vol. 44, No. 3, June 2008.

[19] K. Ma, A.S. Balunan, S.M. Beczkowski, and F. Blaabjerg. *Loss and Thermal Model for Power Semiconductors Including Device Rating Information.* The 2014 International Power Electronics Conference, 2014.

[20] K. Ma and F. Blaabjerg. *Multi-timescale Modelling for the Loading Behaviours of Power Electronics Converter.* Proc. of ECCE 2015, pp.5749-5756, 2015.

[21] P.D. Reigosa, H. Wang, Y. Yang, and F. Blaabjerg. *Prediction of Bond Wire Fatigue of IGBTs in a PV Inverter Under a Long-Term Operation.* IEEE Trans. on Power Electronics, Vol. 31, No. 10, Oct.2016.

[22] Infineon. *Thermal Equivalent Circuit Models: Application Note v1.0.* Infineon technologies AG, Jun.2008.

[23] K. Ma, Y. Yang, and Frede Blaabjerg. *Transient Modelling of Loss and Thermal Dynamics in Power Semiconductor Devices.* Proc. of the 2014 IEEE Energy Conversion Congress and Exposition (ECCE), 2014.

[24] K. Ma, M. Liserre, and F. Blaabjerg. *Reactive Power Influence on the Thermal Cycling of Multi-MW Wind Power Inverter.* IEEE Trans. on Industry Applications, Vol. 49, No. 2, pp.922 - 930, Apr. 2013.

[25] D.A. Murdock, J.E.R. Torres, J.J. Connors, and R.D. Lorenz. *Active Thermal Control of Power Electronic Modules.* IEEE TRANSACTIONS ON INDUSTRY APPLICATIONS, VOL. 42, NO. 2, MARCH/APRIL 2006.

[26] M. Andresen, M. Liserre, and G. Buticchi. *Review of Active Thermal and Lifetime Control Techniques for Power Electronic Modules.* IEEE TRANSACTIONS ON INDUSTRY APPLICATIONS, VOL. 42, NO. 2, MARCH/APRIL 2006.

[27] U.-M. Choi, I. Trintis, Frede Blaabjerg, S. Jørgensen, and M. L. Svarre. *Advanced Power Cycling Test for Power Module with On-line On-state VCE Measurement.* IEEE Applied Power Electronics Conference and Exposition (APEC), Mar.2015.

[28] M. Ciobotaru. *Reliable Grid Condition Detection and Control of Single-Phase Distributed Power Generation Systems.* Aalborg: Institut for Energiteknik, Aalborg Universitet, 2009.